A Study of Meteorological Radar Network at Ku-band with High Resolution

Eiichi Yoshikawa

Department of Information and Communications Technology
Division of Electrical, Electronic and Information Engineering
Graduate School of Engineering, Osaka University, Japan

January 2011

Preface

This thesis presents a meteorological radar network at Ku-band with high resolution. The contents of the thesis are based on the results of my research during the Ph.D. course at the Division of Electrical, Electronic, and Information Engineering, Graduate School of Engineering, Osaka University.

A small-baseline weather radar network is a new strategy to detect small-scale weather phenomena such as tornadoes and downbursts, which often cause damage to our lives seriously. It is difficult for conventional long-range radars at S-, C-, and X-band to detect these small-scale phenomena due to several technical problems. For example, a resolution of a conventional radar (range resolution of 100 m and temporal resolution of 5 min, roughly) is not sufficient to detect these small-scale phenomena (e.g. a tornado has a damage path width of a few hundreds of meters and a duration of 10-20 min). In the most observable area, a long-range radar can not detect anything in the lowest altitudes due to earth's curvature, in which these small-scale phenomena occur. On the other hand, a weather radar network consisting of a Ku-band broadband radar (BBR), which we have been proposing and developing, can observe these phenomena with high accuracy and detection efficiency. The BBR is a short-range pulse-Doppler radar with remarkably high resolution to detect and analyze them. The small coverage is almost never affected by earth's curvature, and the distributed radars cover a wide area. Additionally in the radar network installation, a weather phenomenon in overlapped areas is multi-directionally observed by several BBRs, and physical parameters in the areas are estimated with higher accuracy.

The thesis consists of six chapters that are organized as follows:

Chapter 1 is the introduction of the thesis. Conventional meteorological radars for various applications are described briefly. Compared with them, the motivations and significances of our study are clearly shown.

In Chapter 2, a basic concept, configuration, signal processing, and general parameters of the BBR are presented. In the initial observation results, a cross validation with a ground-based equipment of a disdrometer for assessment of the observation accuracy showed an excellent agreement. Also, in a rain event in Tanegashima island, Kagoshima, it was confirmed that weather phenomena were observed by the spiral observation mode of the BBR with higher resolution than conventional radars.

In Chapter 3, an algorithm applied for the real-time operation in the BBR is presented. The BBR is more affected by ground clutter (reflections from ground, building, trees, and other static targets) than conventional radars since the observable range is very low and the

BBR is occasionally installed in an urban or rugged mountainous area. In many methods proposed for ground clutter suppression, any method with high accuracy has also high computational costs. The algorithm proposed in this chapter suppresses ground clutter and estimates precipitation profiles, even when precipitation echo are overlapped with strong clutter in spectral domain. With assuming a Gaussian spectrum of precipitation and without high-cost calculations such as an inversion of a large matrix, a high accuracy and computational efficiency of this algorithm were achieved and assessed by both simulations and observational experiments.

In Chapter 4, a scientific topic derived from observations on the BBR is presented. Vertical structure of raindrop size distribution (DSD) in atmospheric boundary layer is important to understand observational errors in radar observations. Especially, it is also important for a study of global water cycle using a space-borne precipitation radar. However, it is difficult for all the conventional weather radars, including wind-profilers, and space-borne radars, to observe precipitation below an altitude of several hundred meters. The BBR observation provided the first report that the growth process increases about 2 times in the number of raindrops larger than 0.5 mm in diameter even below an altitude of 300 m in a convective event.

Chapter 5 describes the deployment and characteristics of the BBR network installed in Osaka. At present, two BBRs are deployed and one more BBR will be equipped in next year, 2011. Initial results of simultaneous observations from the two BBRs are shown. The observation results of both BBRs are integrated in an indicated manner, and high-quality images of precipitation are output by complimenting each other. Also, a correction method for precipitation attenuation for the BBR network is presented. Precipitation attenuation is a critical and inherent problem for most precipitation radars since it often yields a large negative bias error which makes us underestimate reflectivity factor of precipitation. Therefore, it is essential for the BBR network to accurately correct precipitation attenuation since Ku-band waves are strongly attenuated more than those lower frequency bands. In a radar network with high temporal resolution, it is likely that precipitation does not change in a volume scan and physical parameters in a point seen from each radar are equivalent. A proposed method in this chapter corrects precipitation attenuation in a stochastic sense. It was presented in a simulation that stochastic properties allow us to optimally integrate precipitation profiles retrieved in each radar in this method.

Finally, Chapter 6 concludes and summarizes this thesis, the results, and the future works.

Acknowledgement

First, I would like to express my sincere gratitude to my supervisor, Professor Zen-Ichiro Kawasaki of Graduate School of Engineering, Osaka University, for his encouragement, valuable discussions, and meaningful advices throughout my studies. His many constructive comments and kind advices have greatly improved this work.

I am much indebted to Professor Shozo Komaki of Graduate School of Engineering, Osaka University, who have given me many insightful suggestions for the thesis as an official reviewer. I take pleasure in thanking Professors Kenichi Kitayama, Tetsuya Takine, Noboru Babaguchi, Seiichi Sampei, and Kyou Inoue of Graduate School of Engineering, Osaka University, and Professors Takashi Washio and Riichiro Mizoguchi of Institute of Scientific and Industrial Research, Osaka University for providing thoughtful comments on this work.

I am deeply grateful to Associate Professor Tomoo Ushio of Graduate School of Engineering, Osaka University for giving me a chance to study in Osaka University, his encouragement, discussions, and advices throughout my studies.

I take pleasure in thanking Dr. Takeshi Morimoto, Dr. Satoru Yoshida, Professor Kenji Yamamoto, and Dr. Gwan Kim of Graduate School of Engineering, Osaka University for helping me a lot to carry out this work.

I would like to thank Professor Yasushi Fujiyoshi of Institute of Low Temperature Science, Hokkaido University for providing with the data of 2DVD and giving me meaningful advices.

I am very grateful to Dr. Tomoaki Mega of Research Institute for Sustainable Humanosphere, Kyoto University and Dr. Satoshi Kida of Kyoto University for a lot of useful discussions.

I also would like to thank Christopher J. Biagi of University of Florida for discussions and English correction.

I would like to express my sincere appreciation to Katsuyuki Imai, Takao Nakagawa, and Yasuhiko Ura of Sumitomo Electric Industries, Ltd., and Shin'ichiro Nagayama and Yoichiro Kato of NEC engineering, Ltd. for developing the BBR and helping our field observation campaigns in Tanegashima island, Kagoshima from 2008 to 2009, and in Osaka from 2009.

I am so much obliged to say thank you to all members of Kawasaki laboratory for their continuous encouragement and meaningful discussions. Special thanks go to Manabu Akita, Hiroshi Kikuch, Yuji Takayanagi, Saku Ieuji, Masatoshi Aoki, Naohiko Wakayama, and Shigeharu Shimamura. And I also thank to Professor Ken'ichi Okamoto (he is

presently with Tottori University of Environmental Studies), Dr. Shoichi Shige (he is presently an associate professor with Kyoto University), Kazushi Monden and all member of Okamoto laboratory of Aerospace Engineering, Osaka Prefecture University. Special thanks go to Shunsuke Noda. Without his help, I did not have chance to study and accomplish this thesis.

Finally, I heartily thank my family, for their patience and support during this demanding period.

Contents

Chapter 1

Introduction

1.1 Radar meteorology

"Radar" stands for radio detection and ranging, whose original purpose is to detect and locate military targets. A radar radiates electromagnetic wave from an antenna to propagate in space. Some of radiated wave is intercepted by a reflecting object located at a distance from the radar. The wave intercepted by the target is re-radiated in many directions. Some of re-radiated wave (echo) is returned to and received by the radar antenna. After the received signal is amplified by several amplifier in a receiver and applied to appropriate signal processing, information of targets are acquired. The echo informs that targets are present. In addition, the signal processing gives us other information directly or indirectly, for example, velocity of moving target [1].

Meteorological radar is designed to give us meteorological parameters of atmosphere. Meteorological radars are designed appropriately and peculiarly for a detection of raindrops, winds, cloud particles, or aerosols. A pulse-Doppler radar for precipitation is the most typical in meteorological radars, whose basic configuration is shown in Figure 1.1. Signals generated in a transmitter pass through a duplexer and are radiated by an antenna in a narrow beam width. Received signals also pass through the duplexer and are input into a receiver. The duplexer blocks out direct inputs from the transmitter to the receiver. Doppler shifts are extracted in a phase detector. Positions, sizes, shapes, and materials of targets determine received power. A distance from the radar is estimated from a time between a transmitted and a received signal. A Doppler shift of the received signals from moving targets is interpreted to a radial velocity.

Meteorological radars play an important role for atmospheric researches. Rainfall observation using a precipitation radar has the major advantage that it is possible to observe widely in a short time, unlike other equipments such as a rain gauge, a disdrometer, or a radiosonde, which obtain physical parameters only at a point. Most meteorological radars observe precipitation, commonly covering 100-450 km in radius with a range resolution of more than 100 m. Indeed, a precipitation radar has capability to spatially map precipitation fields in an atmospheric system, and is an important instrument for understanding atmospheric phenomena. While a non-coherent radar measures only power and range, a

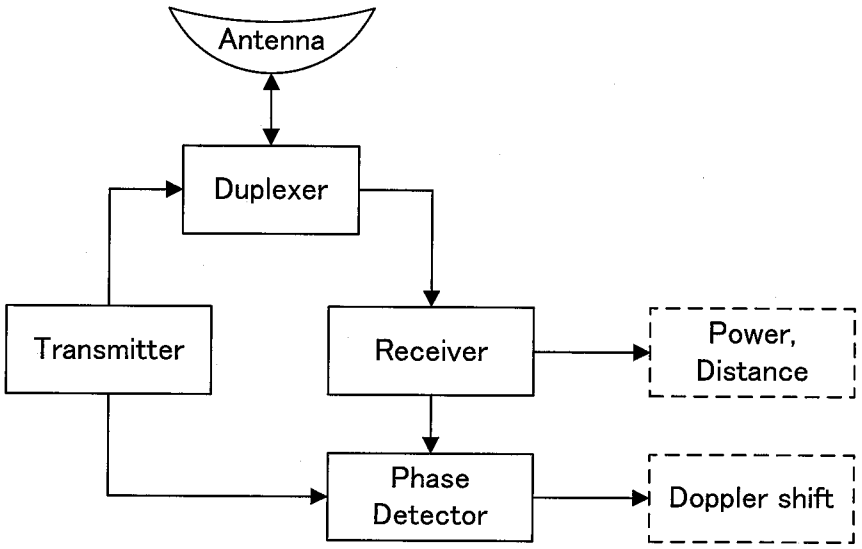

Figure 1.1: Simple configuration of a pulse-Doppler radar. Solid and dashed boxes indicate devices and outputs, respectively.

coherent radar, which transmits coherent pulses, also detects Doppler shifts, and is called a Doppler radar. A polarimetric radar transmits orthogonally polarized waves, and extracts horizontally and vertically polarized waves from received signals. A motion, shape, and phase of precipitation particles are estimated by differences between horizontally and vertically polarized waves. Thus, precipitation radars obtain not only rainfall rate (corresponding to reflectivity) but also various information of a precipitation structure. Ground-based precipitation radars typically transmit electromagnetic waves with a wavelength around 10 cm (S-band), 5 cm (C-band), or 3 cm (X-band). Space-borne radars, Precipitation Radar (PR) (which is loaded on the Tropical Rainfall Measuring Mission (TRMM) satellite) operated at a wavelength of roughly 2 cm (Ku-band), and Dual-frequency Precipitation Radar (DPR) (which will be loaded on the Global Precipitation Measurement (GPM) satellite) operated at roughly 2 cm (Ku-band) and 1 cm (Ka-band), observe precipitation for understanding water cycle on a global scale.

A meteorological radar with a very short wavelength of several millimeters are useful to detect cloud particles. "Lidar", which stands for light detection and ranging, uses laser light to observe atmospheric aerosol particles. However, these short frequency waves are too highly attenuated by precipitation to use in a heavy rain event. On the other hand, a long-wavelength radar, which uses a wavelength from several tens of centimeter to several meters (VHF or UHF-band), called wind profiler, can observe not only precipitation but also motions of clear air. However, interferences are a big problem for atmospheric researches in some cases since many frequencies in these long-wavelength bands are used for broadcasting, and communication.

Nowadays, many atmospheric radars using appropriate wavelengths for the applications of the atmospheric researches have been being deployed. In addition, most atmospheric radars are used for an operation of weather forecasts and nowcasts, and a delivery of warning information, as important infrastructure. The field of radar meteorology has evolved around the development of techniques for deriving meteorological information from measurements [2].

1.2 The Ku-band broadband radar

In Japan, destructions caused by small-scale phenomena have been reported every year. For example, the tornado of F1 scale occurred on Oct. 15, 2010 in Tainai, Niigata, and caused both the human suffering and property damage. Also, it is considered that the derailment in JR Haetsu line, in Shonai, Yamagata in 2005 winter was caused by a microbursts. These weather phenomena had hardly been observed by equipments around, and also never been predicted. Thus, conventional precipitation radars do not have enough capability for detection with high accuracy and probability.

As shown in Figure 1.2, weather phenomena are classified to micro-, meso-, or macro-scale, corresponding to horizontal scale. It is known that horizontal scale of weather phenomena is roughly proportional to their temporal scale. Hazardous weather phenomena such as tornadoes, and microbursts, which often cause damage to our lives seriously, have a small-scale spatially and temporally, as classified into micro-scale [3]. Due to their range resolution of 100 m and temporal resolution of 5 min, a conventional precipitation radar is appropriate for precipitation systems of macro- or meso-scale. On the other hand, it is difficult for a conventional radar to detect smaller scale weather phenomena owing to the low resolution. For smaller scale weather phenomena, for example, a tornado, a conventional radar can obtain few planar structures only which occur near the radar site by coincidence because of 10-20 min mostly or several dozen minutes at the longest and the damage path width of about a few hundreds of meters [4], [5].

The Ku-band broadband radar (BBR) is a ground-based Doppler radar with remarkably high resolution to detect and analyze these small-scale weather phenomena. The BBR transmits and receives wide-band signals at Ku-band to use pulse compression, which gives us sufficient energy on a target for detection with a high range resolution of several meters and a signal-to-noise ratio (SNR). A high SNR achieved by pulse compression reduces to integrate coherent or incoherent pulses and allows us to scan over the whole sky (30 elevations) within a short time of 1 minute. With use of a bistatic antenna system to reduce a direct coupling level and not to turn a receiver off during its transmission, the BBR observes from a minimum detectable range of 50 m to a maximum range of 15 km. These capabilities of the BBR are appropriate to observe small-scale phenomena particularly enough. In Chapter 2, the concept, configuration, and signal processing of the BBR are presented. An accuracy of the observation for precipitation is assessed by a cross validation with a ground-based equipment of disdrometer. Initial observation results in rain events in Tanegashima island, Kagoshima, and Toyonaka city, Osaka, Japan

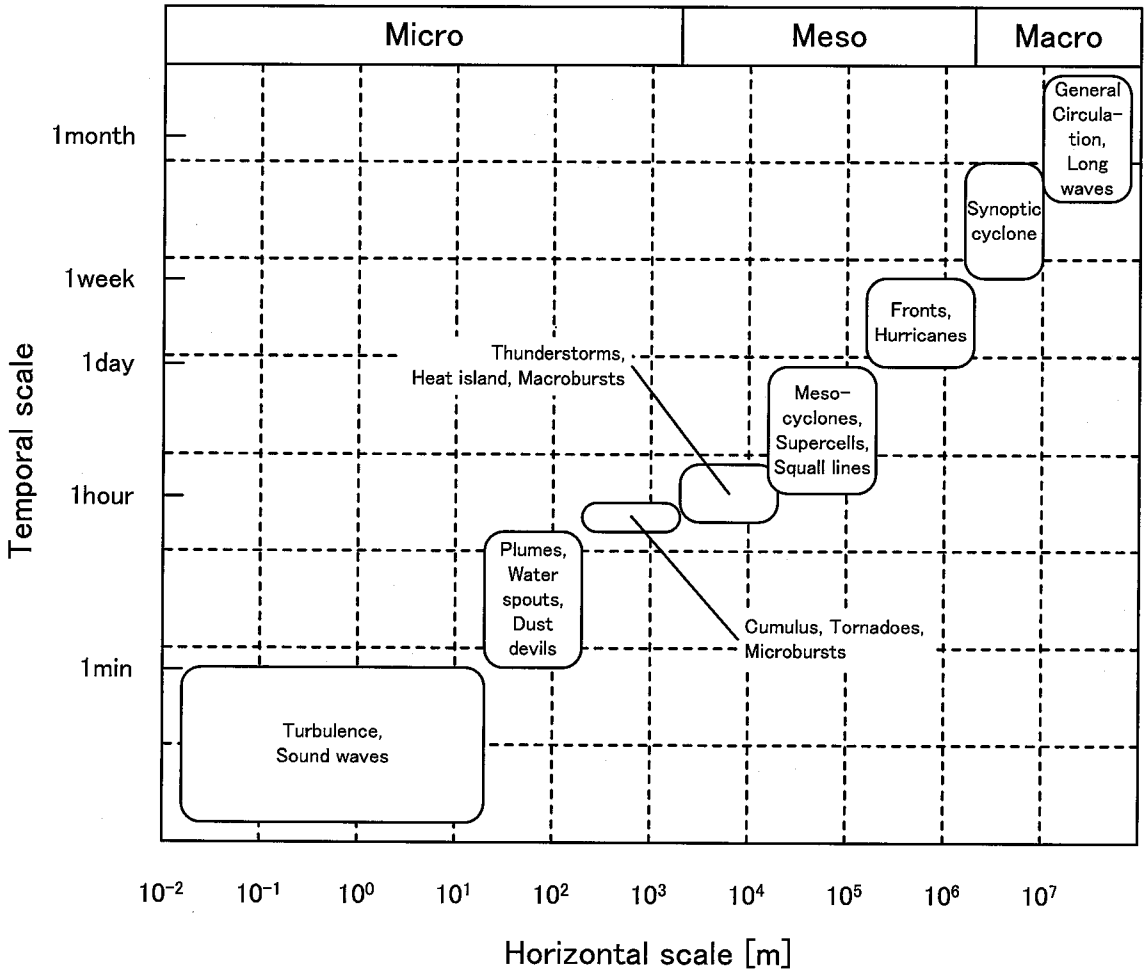

Figure 1.2: Relation of weather phenomena between horizontal and temporal scales.

are also shown.

Since an antenna pattern have not only a main-lobe but also side-lobes, received signals include reflections from undesired targets, such as ground, sea waves, and so on. In order to observe precipitation accurately, it is necessary to suppress these signals returned from these undesirable targets. In Chapter 3, an algorithm to suppress ground clutter (reflections from ground, building, trees, and other static targets) is presented. The BBR is more affected by ground clutter than conventional radars since the observable range is very low and the BBR is occasionally installed in an urban or rugged mountainous area. Though many methods for ground-clutter suppression have already been proposed, methods with high accuracy have also high computational costs. The algorithm proposed in this chapter suppresses ground clutter and estimates precipitation profiles, even when precipitation echo are overlapped with strong clutter in a Doppler frequency domain, with a low computational cost to perform in the real-time observation of the BBR.

In Chapter 4, a scientific topic derived from observations of the BBR is presented.

Previous studies [6], [7] used co-located wind profilers and disdrometers to study the localized features of vertical precipitation profile and uncertainties in radar observations of precipitation. Such studies indicate that changes in precipitation profiles, such as water vapor, can be significant in the ABL. Such changes in precipitation profiles results in observational errors in radar observations near ground. Precipitation profiles in the ABL are important as ground validation of PR products of the TRMM satellite, particularly when studying the global water cycle [8]. However, since conventional radars cannot observe below altitudes of several hundred meters (about 300 m at least) and operational radars focus on even higher altitudes, precipitation profiles in the lower ABL (under 300 m) are typically not observed by radar. This is the first reports about the profiles in the lower ABL below 300 m observed by the BBR.

1.3 Meteorological radar network at Ku-band with high resolution

A small-baseline weather radar network is a novel strategy to detect small-scale weather phenomena such as thunderstorms, tornadoes, and downbursts. Collaborative Adaptive Sensing of the Atmosphere (CASA) [9] and X-band radar network (X-net) [10] have proposed a new radar network system using short-range X-band radars to observe lower troposphere. Compared with them, we have been proposing a weather radar network consisting of the BBR, a shorter-range and higher-resolution radar than X-band radars.

Conventional radar network with long-range radars covering over 100 km in radius has disadvantages in detection for small-scale phenomena. In addition to the spatial and temporal resolution as stated in the previous section, it is difficult for a long-range radar to choose a site for the installation. This is because any obstacles must be excluded to radiate pulses in an low elevation angle and observe in low altitude as possible. Even if being installed in an ideal location, as shown in Figure 1.3 (b), a long-range radar have unobservable area in the lowest altitudes. Due to earth's curvature, a radar beams overshoot in a higher altitude in a longer range, even when an antenna elevation is set to 0 degree [11].

On the other hand, the BBR network have unique advantages. In addition to the remarkably high resolution, because of the observable range from 50 m to 15 km, the BBR almost never have unobservable areas without the effect of earth's curvature, and efficiently observes only troposphere as shown in Figure 1.3 (a). It is easy for the BBR to be installed in an urban or mountainous areas since an unobservable area of one BBR in low altitudes generated by an obstacle can be observed by another BBR deployed appropriately for surrounding environment. Also, it is likely for the BBR network to assume that measurements at a point are simultaneously observed by several BBRs due to the high temporal resolution. The multiple measurements at a point contribute to estimate precipitation parameters more accurately.

Chapter 5 describes the deployment and characteristics of the BBR network installed in Osaka. Also, a correction method for precipitation attenuation for the BBR network is

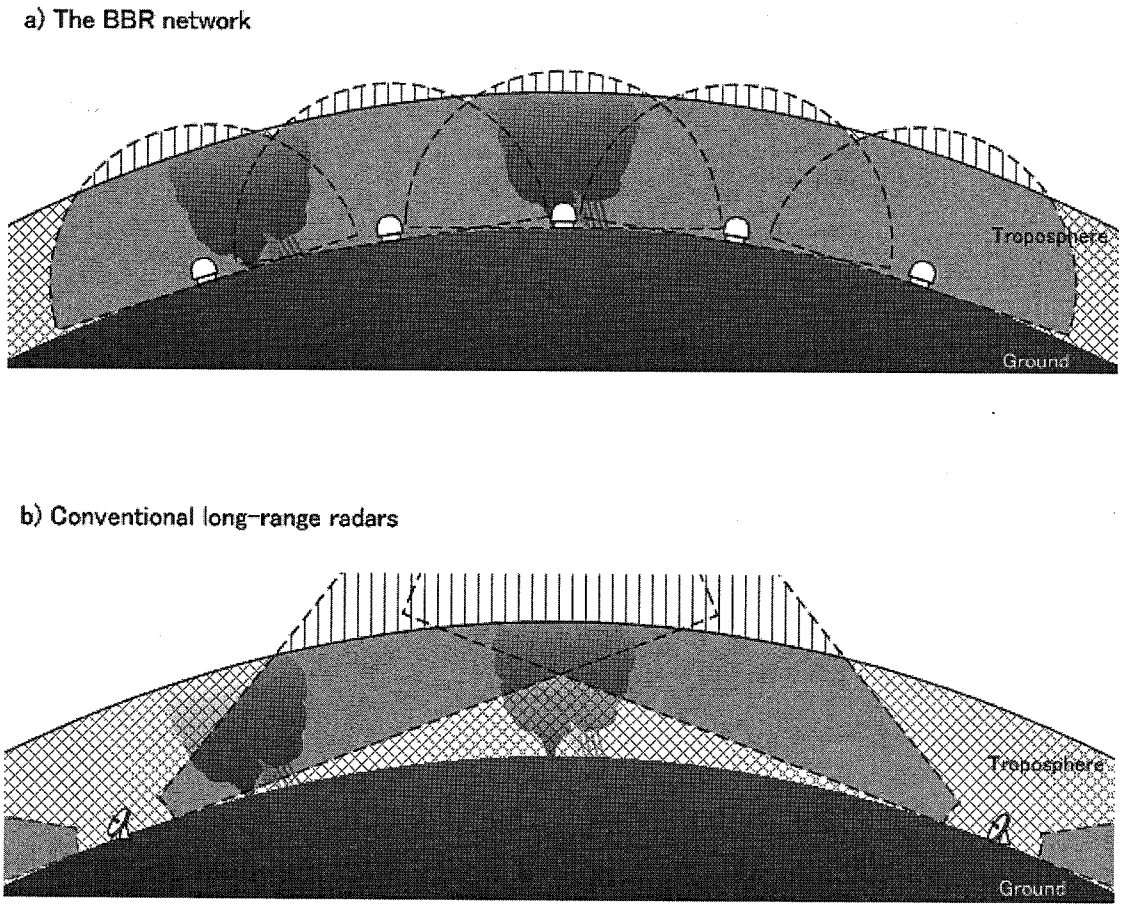

Figure 1.3: Descriptional comparison between the BBR network and conventional long-range radars

presented. Precipitation attenuation is a critical and inherent problem for most precipitation radars since it often yields a large negative bias error which makes us underestimate reflectivity factor of precipitation. Therefore, it is essential for the BBR network to accurately correct precipitation attenuation since Ku-band waves are strongly attenuated more than lower bands (for example, S-, C-, or X-band, which are used by conventional precipitation radars). As mentioned above, it is likely to assume that precipitation does not change in a volume scan of 1 min and physical parameters in a point seen from each radar are equivalent. A proposed method in this chapter corrects precipitation attenuation in a stochastic sense. Stochastic properties allow us to optimally integrate precipitation profiles retrieved in each radar. It is confirmed by using both simulation models and initial observations of the BBR network that this approach provides accurate and stable retrievals.

Chapter 2

The Ku-band broad-band radar

2.1 Introduction

We have been developing the Ku-band BBR, a remarkably high-resolution Doppler radar for meteorological application to detect and analyze small-scale weather phenomena, such as tornadoes, and downbursts, which often cause damage to our lives seriously. This chapter presents development and observations of the BBR. Section 2.2 shows basic concepts, configuration, and signal processing of the BBR. Section 2.3 shows initial observation results and assessments of an estimate accuracy by a cross-comparison with a ground-based equipment of disdrometer. Section 2.4 discusses the observation results and summarizes this chapter.

2.2 The Ku-band broadband radar

2.2.1 Basic concept

It is well known that smaller scale weather phenomena, such as localized scattered thunderstorms, tornadoes, and microbursts, have a few hundreds of meters horizontal scale and several dozens of minutes duration or several ten meters and several minutes for smaller ones. These phenomena are accompanied by precipitation and occur under a cloud whose base altitude is below 2 km. Therefore, in order to analytically study and practically detect inner fine-scale behaviors of precipitation inside these phenomena, a volume-scanning radar, which observes with a high resolution of several meters and several tens of seconds per volume scan (VoS) from a low altitude as possible, is needed. The target value of sensitivity is set to 20-dBZ reflectivity (which is roughly equal to 1 mm h^{-1}, corresponding to the capability of a usual rain gauge) to observe precipitation particularly in severe weather.

The BBR transmits and receives wide band (80 MHz (max)) signals at Ku-band (15.75 GHz) to use pulse compression, which gives us sufficient energy on a target for detection with high range resolution and signal-to-noise ratio (SNR). The high SNR achieved by

pulse compression reduces to integrate coherent or incoherent pulses and allows one to scan over the whole sky with a high speed of 55 s per VoS. The high range resolution and the low coupling level (-70 dB) enable the BBR to observe precipitation profiles from a range of 50 m. In order to compensate the strong precipitation attenuation at Ku-band, the BBR is designed as a close-range radar to 15 km for precipitation above 20-dBZ reflectivity with low-power transmission (10W). Due to the close-range system design and using Ku-band components, the cost of the whole system is reduced, and the system size is miniaturized in order to be installed easily. The BBR is equipped with solid-state components, GaAs power devices, as the transmitter because of the longer lifetime and the lower maintenance cost than magnetrons or klystrons. Since the maximum output power of GaAs power device at Ku-band is several watts currently, the parallel composition of four GaAs power devices achieves a transmission power of 10 W.

Precipitation attenuation

Shorter wavelength radars suffer from more power loss of scattering and absorption of electromagnetic waves by a water particle. The solution for backscattering cross section and absorption cross section for a water particle of a dielectric sphere is due to the Mie theory, which indicated that these cross sections depend on the diameter of a water particle, complex index of refraction for liquid water, and transmitting wavelength. Equivalent reflectivity factor and precipitation attenuation are respectively expressed as the accumulations of backscattering cross sections and extinction cross sections for all radiated rain drops (extinction cross section is the sum of absorption and backscattering cross sections) [13], [14]. In Figure 2.1, the relations between reflectivity factor and precipitation attenuation at C-, X-, Ku-, and Ka-bands calculated due to Mie solution from raindrop size distribution (DSD) observed by 2-D video disdrometer (2DVD) [15] are shown. Electromagnetic waves at Ku-band are attenuated over four to six times more than those at X-band. Therefore, the BBR is designed as a close-range radar with a maximum detectable range of 15 km. When precipitation with a reflectivity factor uniformly exists all over a pass, total attenuations in each maximum range at each frequency band are shown in Figure 2.2. The maximum ranges of C- and X-band radars are assumed as 450 and 80 km, respectively. As a reference, precipitation attenuation at Ka-band at a range of 15 km is also shown. The effect of precipitation attenuation for a Ku-band radar is as much as that for X-band in all reflectivity, and frequencies higher than Ku-band are significantly affected by precipitation attenuation.

2.2.2 Configuration

The schematic diagram and the specification of the BBR system are shown in Figure 2.3 and Table 2.1, respectively. In the BBR, the transmission source is a digital-to-analog converter (DAC) with a maximum sampling frequency of 170 MHz and a vertical resolution of 14 bits. The digital data of the transmitting waveforms, an in-phase (I) channel, and a quadrature-phase (Q) channel are input in a personal computer in ASCII text

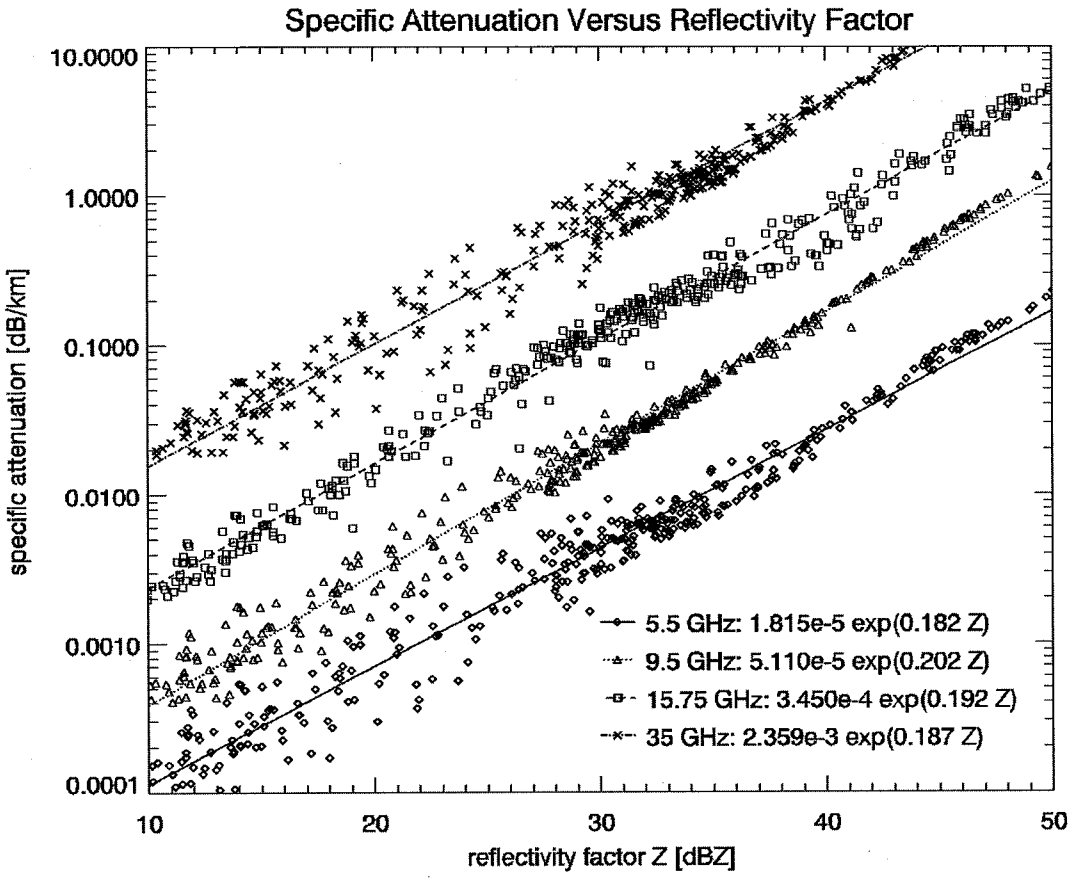

Figure 2.1: Specific attenuation versus reflectivity factor: Diamond, triangle, square, and x marks indicate the equivalent reflectivity factors and specific attenuations, respectively, at 5.5, 9.5, 15.75, and 35 GHz calculated by Mie equation from DSDs of 2DVD. Solid, dotted, dashed, and dotted-dashed lines denote the linear approximations at 5.5, 9.5, 15.75, and 35 GHz, respectively.

format. The I and Q transmitting signals are combined, amplified, and up-converted to 2-GHz band as the intermediate frequency on the IQ modulator and a neighboring amplifiers. Using the 2-GHz band, whose components are abundantly provided, facilitates the reduction of cost. The combined signal is additionally up-converted to 15.75 GHz and amplified to 10 W in the amplifiers, and the mixer is installed immediately below the antennas. Then, the signals are transmitted by the antenna elaborated hereinafter. The scattered signals are received, down-converted, and then divided into I and Q signals at baseband. The analog-to-digital converter (ADC), with the same sampling frequency and vertical resolution as the DAC, samples the received signals of I and Q in linear scale. After the digital sampling, the signal-processing unit performs the digital signal processing in real time.

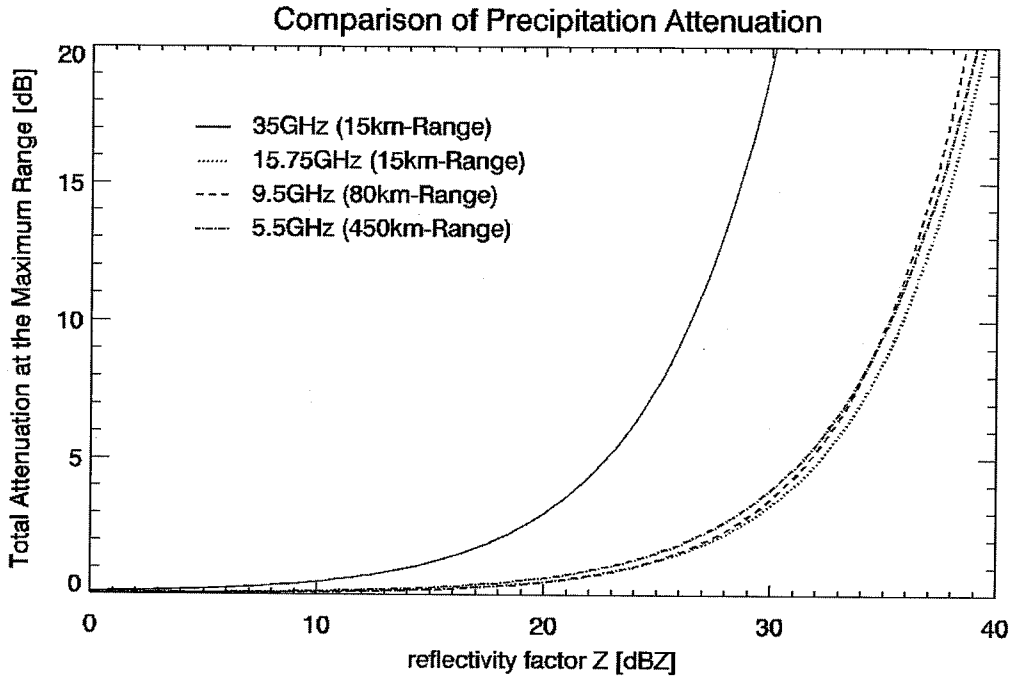

Figure 2.2: Comparison of total path precipitation attenuation at maximum detectable range: Solid, dotted, dashed, and dot-dashed lines indicate the total attenuations with a reflectivity factor existing all over the paths whose lengths are 300 km at 5.5 GHz, 80 km at 9.5 GHz, 15 km at 15.75 GHz, and 15 km at 35 GHz, respectively.

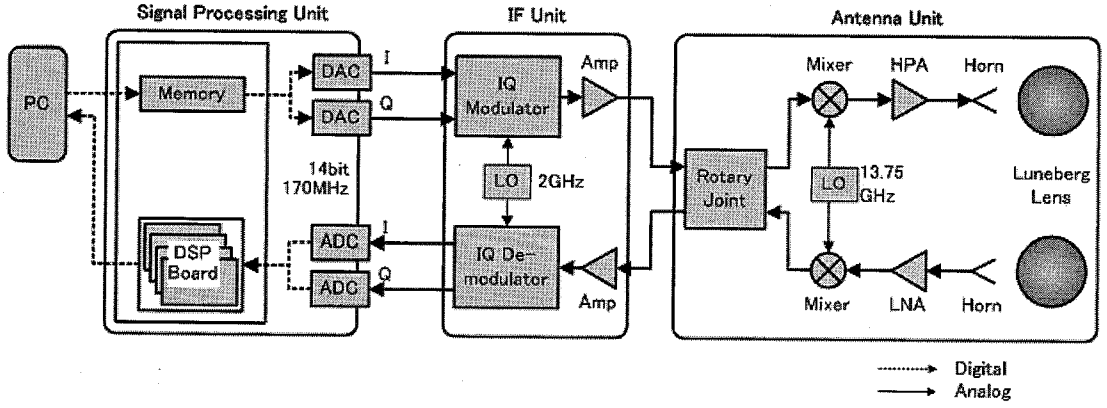

Figure 2.3: Schematic diagram of the BBR. (HPA) High-power amplifier. (LNA) Low-noise amplifier. (LO) Local oscillator.

Antenna system

Most weather radars have a monostatic antenna system because of simplicity. However, monostatic systems must use a duplexer just before the antenna to switch the trans-

Table 2.1: Specification of the BBR

	Item	Specification
System	Operational frequency	15.71 - 15.79 GHz
	Operation mode	Spiral,Conical, and Fix
	Band width	80 MHz (max)
	Coverage Az / El	0 - 360 / 0 - 90°
	Azimuth rotation speed	40 rpm (max)
	Weight (only antenna driving part)	500 kg
	Size (only antenna driving part)	ϕ1600 mm - 1700 mmH
Antenna	Gain	36 dBi
	Beam width	3°
	Polarization	Linear
	Cross polarization	25 dB (min)
	Noise temperature	40 K (typical)
Transmitter and Receiver	Transmission power	10 W (max)
	Duty ratio	Variable
	Noise figure	2 dB (max)
Signal Processing	Digital to analog converter	170 MHz (max) / 14 bits
	Analog to digital converter	170 MHz (max) / 14 bits
	Range gate	32768 points
	Pulse repetition time	Variable

mission and reception. The low transmission-to-reception isolation level restricts the dynamic range or forces the system not to obtain the low-range data. In particular, in a pulse compression radar which transmits long time modulated pulses, the saturation caused by a direct input from the transmitter side makes wide unobservable area. Therefore, sufficient low coupling level is necessary for the BBR to observe at low ranges. In addition, a quite high speed (20-40 r min^{-1}) and a robust scanning system are also necessary in order to achieve a high time resolution of 55 s per VoS with full-time operation. Although a mechanical azimuth/elevation (Az/El) drive system with a parabolic antenna is common among most weather radars, this system is complicated and unstable in these rotation speeds. It is suitable for a high-speed scan to use a phased array antenna system. However, a phased array system requires several planar array panels to observe the whole sky because of the beam broadening by more than $\pm 45°$ from the central axis [16].

In the BBR, we adopted a bistatic antenna system with the use of Luneburg lenses [17]. Due to this design, the BBR achieves a mutual coupling level of -70 dB between the transmitting and receiving antennas, which is superior to that of monostatic configuration. As a result, the lowest observable range of 50 m is achieved. Each antenna consists of a primary feed (conical horn) and a 450-mm-diameter Luneburg lens with an antenna gain

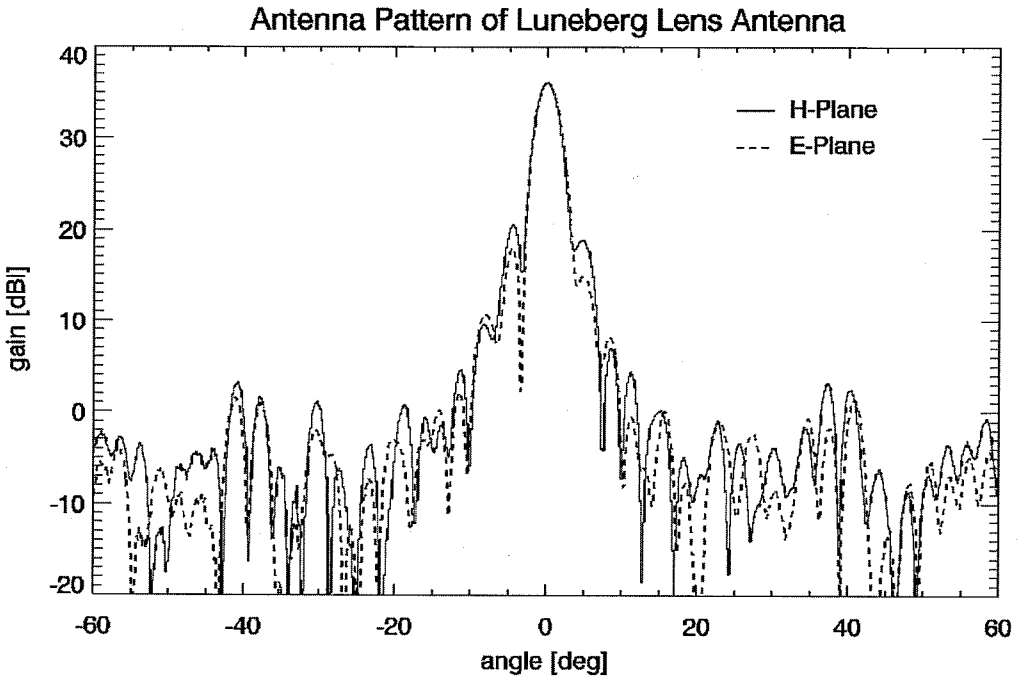

Figure 2.4: Antenna pattern of a 450-mm-diameter Luneburg lens antenna. Solid and dashed lines indicate the H- and E-plane, respectively.

of 36 dBi and a beamwidth of 3° to simplify the antenna rotation mechanism. In this type, the antenna mount rotates at a speed of 40 r min^{-1} (max) for azimuth, and only primary feed moves for elevation. In Figure 2.4, the antenna pattern of this antenna at a frequency of 15.75 GHz is shown.

Basic radar equation

Considering both the antenna gain and the coupling level, two antennas are parallely angled with a baseline length of 550 mm in the BBR. When the antennas are angled parallely, a resolution volume with a long baseline or a sharp beamwidth for observing ranges is elliptically distorted from the sphere pattern, and then, the total antenna gain is significantly reduced from that of monostatic system instead of the lower coupling level. In addition, since the ranges from each antenna to a target are different, the range correction is not equivalent in a same resolution volume. Because it is difficult to determine the propagation lengths of transmitter to target and target to receiver, the range from the center of baseline to a target is used for the range correction.

In order to evaluate the power loss due to nonoverlapping beams and the bias error of the range correction, the radar equation is simulated at the nearest ranges, and the result of total power loss in the bistatic system compared with that of the monostatic system is shown in Figure 2.5. The maximum power loss is a small value of about 0.1 dB at a

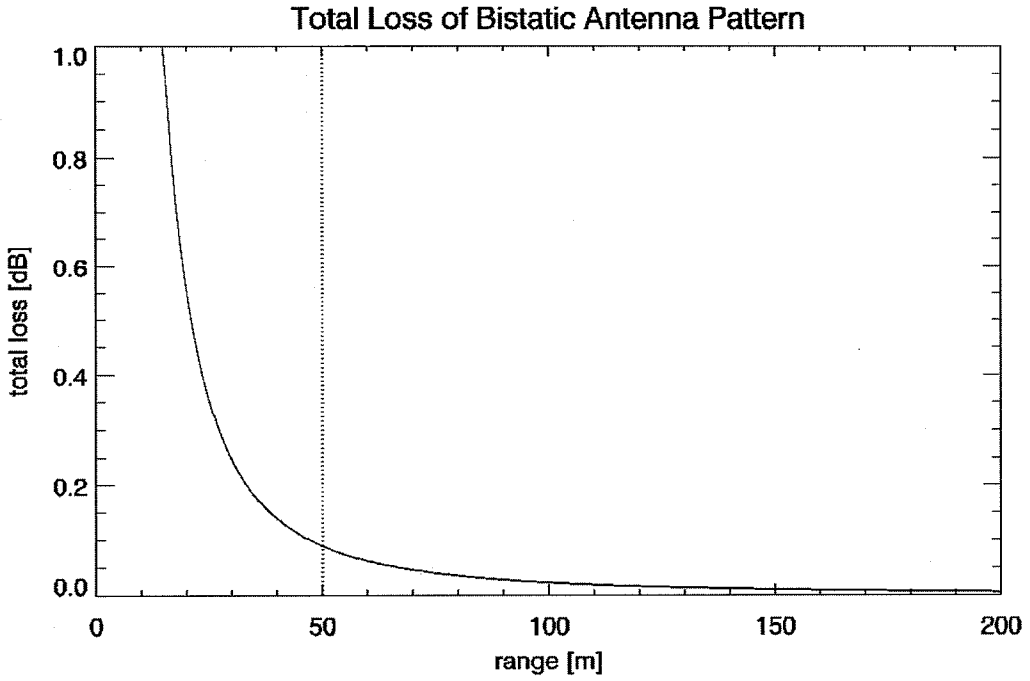

Figure 2.5: Total loss of bistatic antenna pattern, which consists of the non-overlapping beams and the range correction error of the bistatic configuration. The dotted line indicates the minimum detectable range of 50 m.

range of 50 m, and these biases are corrected in the operation. This result is calculated on the assumption that the antenna pattern is approximated by Gaussian with the same beamwidth and gain as the Luneburg lens antenna shown in Figure 2.4 and precipitation is uniform in the resolution volume. Although it is considered that nonuniformity of precipitation particularly contaminates this bias correction, this contamination is invalid at short ranges due to the very small resolution volume. Therefore, it can be said that the BBR antenna system is virtually equal to a monostatic system.

2.2.3 Signal processing

The flow of the BBR signal processing is shown in Figure 2.6. The process is roughly separated to a former process, which processes pulse compression, and a latter process, which processes Doppler moment estimation.

To achieve the VoS (3600 directions and 64 pulses per direction) in a time resolution of 55 s per VoS, the interpulse period (IPP) must be within about 239 μs, which contains the range gate points of 2^{15} (32768) in a sampling frequency of about 137 MHz (these observation parameters are elaborated in the next section). That is, the former processor must perform a fast Fourier transform (FFT) and an inverse FFT with 2^{15} points

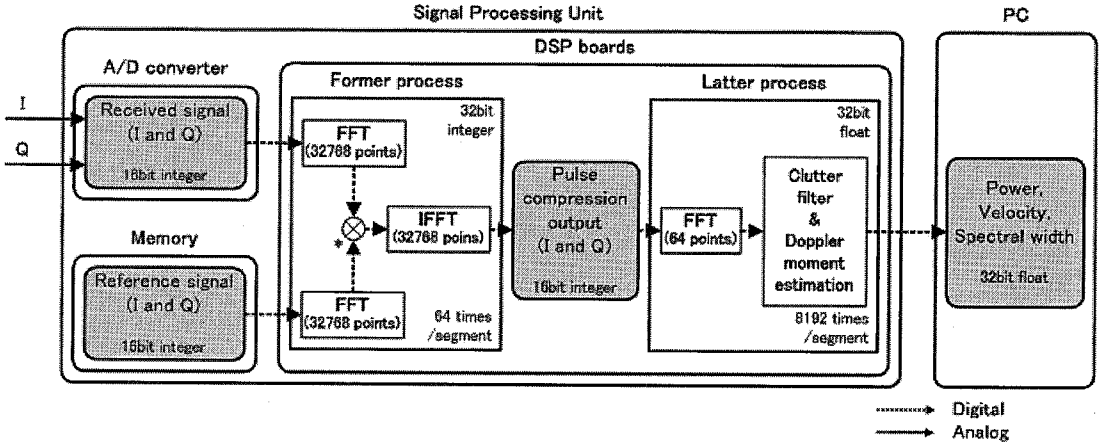

Figure 2.6: Flow of the BBR signal processing.

within an IPP of 239 μs for the real-time operation. Therefore, the BBR signal-processing unit is equipped with 32 digital signal processors (DSPs) of 32-bit integer type, which can rapidly process the FFT, and the DSPs parallely process the received data. Meanwhile, the latter process employs a spectral approach [18]. This approach is developed for remarkable high resolution radars like the BBR, which needs a simple algorithm with high estimate accuracy for the real-time operation. This approach adequately filters ground clutter, which adversely affects the performance of ground-based weather radars, by searching and determining clutter region in the frequency domain and then estimates the first three spectral moments (power, velocity, and spectral width) by corresponding Gaussian to a Doppler spectrum. Also in the latter process, an FFT with 64 points must be performed in 2^{13} (8192) range bins within about 15.3 ms. That is why the latter processor is equipped with six DSPs of float type. Because DSP is superior than other devices such as field-programmable gate array with respect to cost and computational efficiency for an FFT, it is optimum for pulse compression radars using an FFT with many points. The latter process is presented in details in the next chapter.

Pulse compression

In the BBR, the linear up-chirp pulses and a matched filter are generally used for real-time observation. Since the received power is given by the integration of compressed waveforms from distributed particles in a compressed resolution volume, pulse compression does not improve SNR compared with single frequency pulse with the same duration pulses for precipitation radars. The important role of pulse compression for precipitation radar is that a high-power and short-pulse radar, which is difficult for analog design, is realized by configurations with low power and low SNR. In particular, the low SNR does not need an ADC with high vertical resolution and also enables us to reduce computational cost. In the meantime, the ambiguity function of the matched filter output in

using linear up-chirp pulse indicates some potential problems of the time response and range sidelobe. The time response to a rain drop with a radial velocity is expressed as a time-reversed version of the autocorrelation function, and the absolute value linearly increases with f_d/B and t , where f_d is the Doppler shift. In the BBR, this problem is suppressed due to the wide bandwidth. The range sidelobe is also an important problem which reduces the dynamic range of a radar. In order to suppress the range sidelobe, it is an easy way to transmit the modulated pulse weighted a window function. The BBR system generally uses the raised-cosine window function expressed as follows due to the tradeoff between loss in SNR and sidelobe characteristics:

$$w = \begin{cases} 0.5 - 0.5\cos(\alpha t/\pi\tau) & (t \leq \alpha\tau) \\ 1 & (\alpha\tau < t \leq (1-\alpha)\tau) \\ 0.5 - 0.5\cos(\alpha(t-\tau)/\pi\tau) & ((1-\alpha)\tau < t \leq \tau) \end{cases} \tag{2.1}$$

The coefficient α can be substituted with a value from 0.0 to 0.5 (Of course, $\alpha = 0.0$ is not strictly achieved). The performance of the transmitted waveform in the general operating parameters is quantitatively stated in the next section.

2.2.4 General parameters

The general parameter set is described in Table 2.2. The BBR is generally operated in the spiral mode to observe the whole sky with an update rate of 1 min. A beamwidth of 3° can resolve 3600 directions for VoS (120 directions for azimuth and 30 directions for elevation). Considering an antenna reset time of 5 s, the time resolution for 1 VoS is determined to 55 s. Then, the measurement of one direction is allowed within about 15.3 ms. When 64 pulses are transmitted per direction for Doppler spectrum estimation, the IPP is about 239 μs, which is sufficient for the maximum range because the necessary transit time for a 15-km range is about 100 μs. The Nyquist velocity in this IPP and frequency is about 20 m s^{-1}. Then, the effect of scan speed for velocity spectrum width is indicated in [19]. The spectral width due to the antenna rotation is 0.165 m s^{-1} when the rotation speed is 32.7 r min^{-1} when the elevation angle is zero.

Autocorrelation of Transmitting Waveform

In the stand alone operation of the BBR, the transmitting waveform is the linear up-chirp waveform with a usable bandwidth of 80 MHz. Given that B and t are 80 MHz and 139 μs, respectively, the $\alpha = 0.1$ in Eq. 2.1 is appropriate because of the tradeoff between the loss in SNR and sidelobe characteristics. Figure 2.7 shows the comparison of compressed pulse shapes. Note that this figure is a simulation result and not based on the data collected by the BBR. The compressed output powers are normalized by the peak of the output from the unweighted waveform. The 80-MHz linear chirp signal weighted raised-cosine ($\alpha = 0.1$) autocorrelation output has slightly higher levels of sidelobe within 50 m and superior sidelobe characteristics over 50 m compared with the unweighted output.

Table 2.2: General observation parameters of the BBR

Operation mode	Spiral
Coverage Az / El	0 - 360 / 0 - 90°
Azimuth rotation speed	32.7 RPM
Power	10 W (peak)
Transmitting waveform	Liner up-chirp
Sampling frequency	138 MHz
Band width	80 MHz (variable)
Pulse length	139 μs
Inter pulse period	239 μs
Pulses / segment	64
Weighting window	Raised-cosine window ($\alpha = 0.1$)
Pulse compression filter	Matched filter
Resolution (Range)	2 m
Resolution (Time)	55 s per VoS
Nyquist velocity	20 m s^{-1}

The range sidelobe level of the raised-cosine weighted output continues to decrease even after the 100-m range (not presented here). The range sidelobe levels 10, 50, and 100 m away from the peak position are ideally about -25, -65, and -90 dB from the peak level. Although the effects of phase noise and ground clutter would further deteriorate these characteristics, they are rather suppressed in the Doppler frequency domain in the latter process. Loss in SNR and -3-dB mainlobe width are 1.16 dB and 2 m, respectively. It is indicated that these sidelobe levels are sufficiently low to observe small-scale phenomena such as a tornado [20].

Considering to adopt the frequency division principle, which is the easiest solution for the interfering problem in the BBR network operation, the 26.7-MHz chirp signal (in the case of three BBRs) weighted raised-cosine ($\alpha = 0.1$) autocorrelation waveform is also shown. Since the range sidelobe levels increase at all ranges compared with that of 80 MHz, a more aggressive window function, for example, Kaiser window, is necessary to suppress them below the noise level.

Radar Sensitivity

A detectable range is determined by transit time and radar sensitivity. Pulse compression gain $B\tau$ and the compressed range resolution c/B cancel each other, and then, the derived radar equation for pulse compression is not changed compared with normal pulse radar equation. System noise temperature is calculated to -95.6 dBm from the noise temperature of antenna T_a, line T_l (= 290 K), low-noise amplifier T_R (= 110 K), and guide

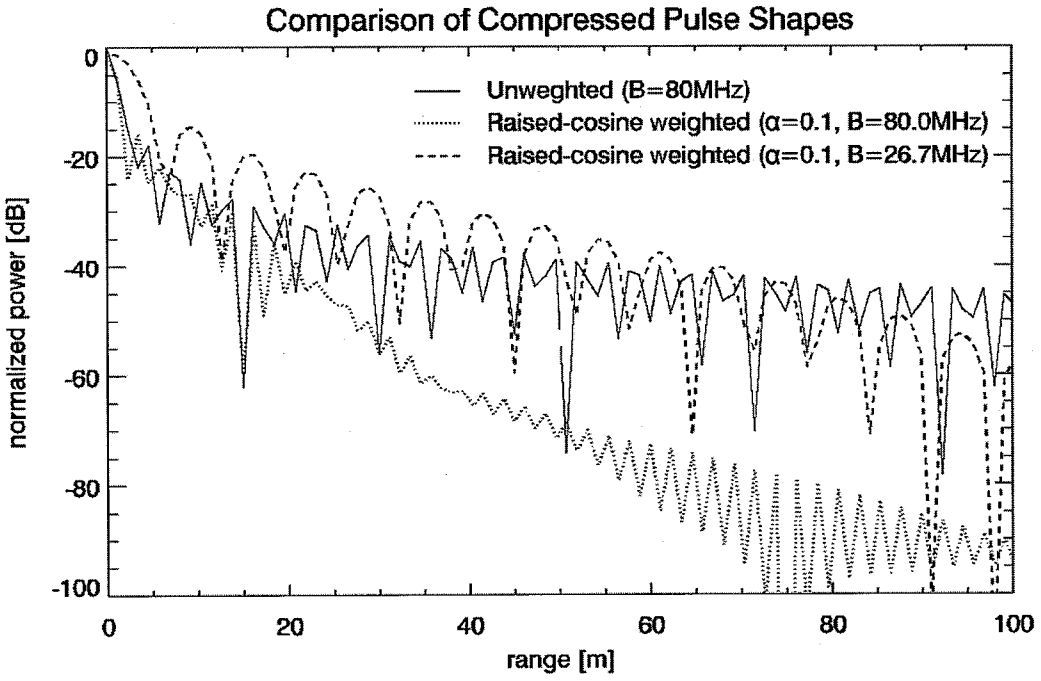

Figure 2.7: Simulation comparison of compressed pulse shapes. Output powers are normalized by the peak power from an unweighted waveform. The solid, dotted, and dashed lines are the output powers from an unweighted waveform with 80-MHz bandwidth, a raised-cosine weighted waveform with 80-MHz bandwidth, and a raised-cosine weighted waveform with 26.7-MHz bandwidth, respectively.

loss l_l (= 1 dB) [21]. Figure 2.8 shows the detectable range of Z_e = 10, 15, and 20 dBZ calculated by the noise level. In addition, the maximum range due to transit time is also shown. This figure indicates that the trade-off of transit time and detectable range of Z_e = 20 dBZ determines the optimal pulse width as roughly 108 μs, which is the crosspoint between the two. In the BBR operation, pulsewidth is set to about 138 μs, which has some amount of robustness for sensitivity (over 5 dB). Although the received power and time response are adversely affected for high-velocity targets in a matched filter, the effects are very small due to the wide bandwidth (respectively, about 0.001 dB and 10 ns for a target with a radial velocity of 70 m s^{-1}).

2.3 Initial observation results

2.3.1 Observation accuracy

In order to confirm the accuracy of the BBR reflectivity profile, we observed a precipitation event in the conical observation mode. Here, the azimuth rotation speed is 30 r

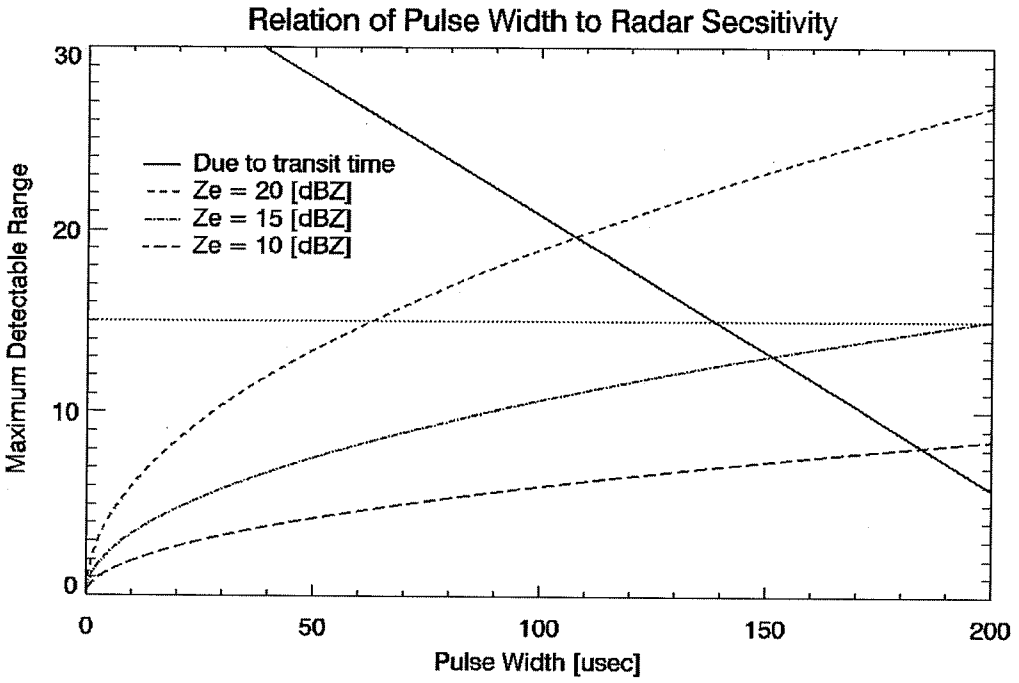

Figure 2.8: Relation of pulsewidth to radar sensitivity. The solid line is the maximum ranges due to transit time. The dashed, dot-dashed, and long dashed lines denote the detectable ranges for the equivalent reflectivity of 20, 15, and 10 dBZ, respectively. The dotted line indicates the 15-km range.

min^{-1}, in which the BBR obtains the data of an azimuth direction every 2 s. The observation characteristics are shown in Observation I of Table 2.3. The observation results of the BBR are compared with the JWD (Joss-Waldvogel Disdrometer; RD-80, Disdromet Inc.) installed roughly 10 m away vertically and horizontally. The observation overview is shown in Figure 2.9.

The JWD is a disdrometer of impact type to estimate DSD accumulated in each minute. Here, an equivalent reflectivity factor Z_e is calculated from the DSD of JWD using the Mie scattering equation every minute. The measured reflectivity factor Z_m of the BBR is calculated by averaging 30 values of power outputs from the signal processor (1-min averaging value) at a range of 50 m for an elevation of 30° and then calibrated by Z_e to eliminate the bias. The scatter plot of comparison between Z_m and Z_e and the histogram of the reflectivity difference are shown in Figures 2.10 and 2.11, respectively, and indicate a fairly good agreement. As evaluated values of the estimate accuracy of the high range resolution with high azimuth rotation speed, the correlation coefficient is 0.95, and the standard deviation is 1.59 dB, except for Z_e under 10 dBZ, which is the sensitivity limit of the BBR at this range. Considering the low propagation loss at 50 m, the sensitivity of 10 dBZ is worse. This is caused by the range sidelobes. Because the

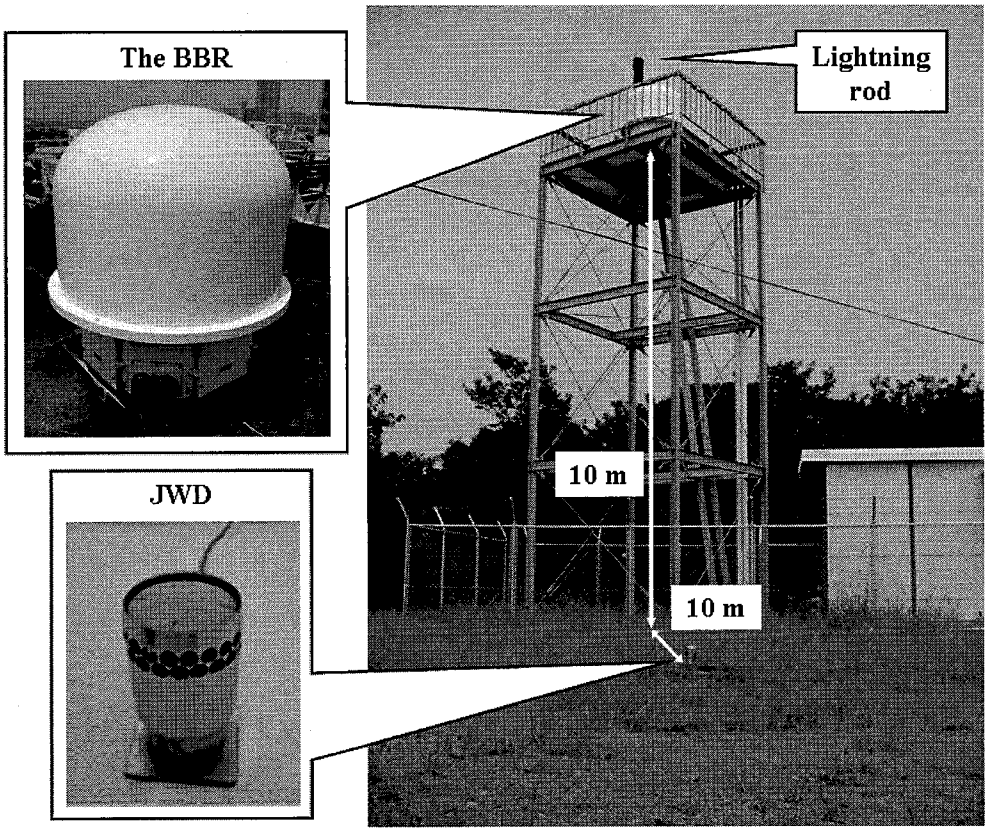

Figure 2.9: Observation overview; the JWD is installed roughly 10 m away horizontally and vertically from the BBR. The lightning rod blinds the observation area around north-east.

BBR uses pulse compression, the range sidelobes of clutter sidelobe due to direct coupling, which depend on the transmitting waveform, are superior to the thermal noise only at short ranges. That is, the sensitivity of 10 dBZ at 50 m means that this transmitting waveform has sufficiently low-range sidelobe. Sensitivity at a longer range is restricted only by the thermal noise, and the value estimated in the observation is stated in the next section.

2.3.2 Spiral observation

We made an initial observation using the BBR of spiral mode. The observation characteristics are shown in Observation II of Table 2.3. This spiral mode observes the 3-D structure of precipitation for 3600 directions with a range resolution of about 4 m. Figure 2.12 shows the Constant Altitude Plan Position Indicators (CAPPIs) every minute from 19:25 to 19:30 (from left to right panels), which are reflectivity factors at altitudes of 2000, 1000, and 0 m (the base scan) and Doppler velocity (mean radial velocity) of the

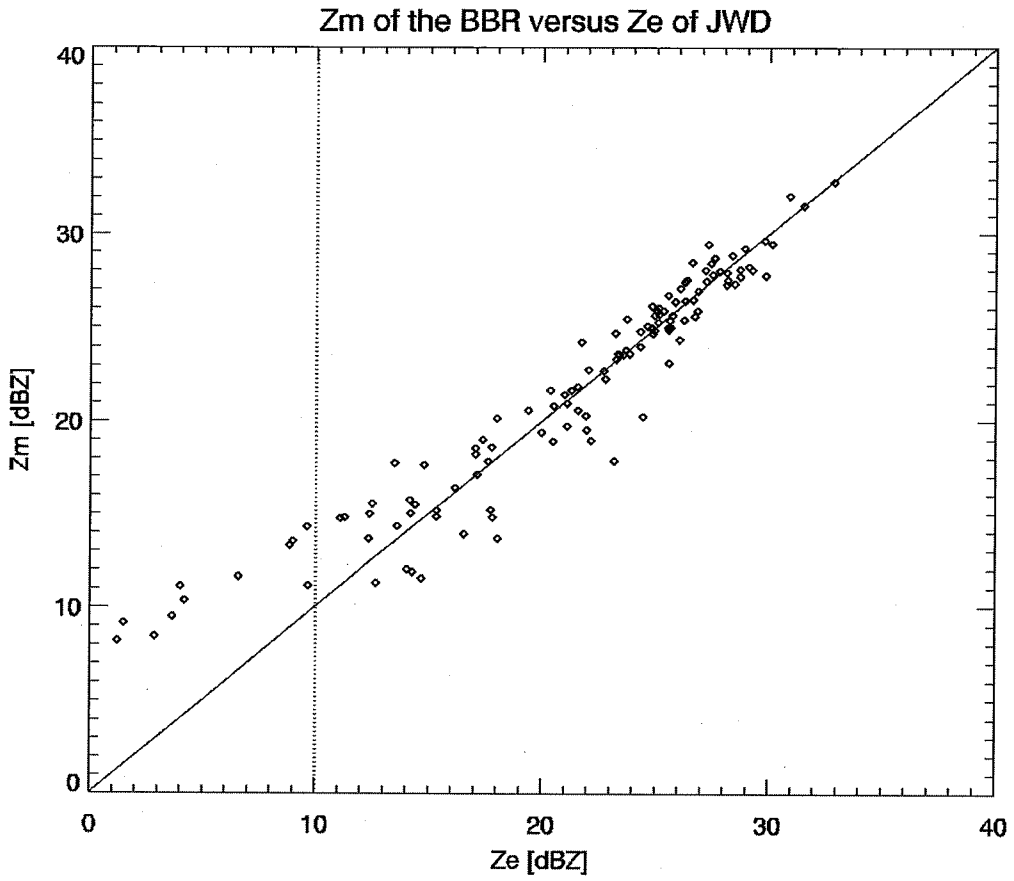

Figure 2.10: Scatter plot of Z_m (BBR) and Z_e (JWD). (Solid line) $Z_m = Z_e$. (Dotted line) $Z_e = 10$ dBZ.

base scan (from top to bottom panels). Note that warm and cold colors indicate the velocities toward and against the BBR in Doppler velocity panels, respectively, and precipitation attenuation is not corrected in reflectivity panels. As shown in Figure 2.9, the BBR cannot observe for some directions around northeast in this site, owing to the lightning rod which must be deployed according to the regulation of this site.

From each panel of 2.12, it is clear that the fine structure of the thunderstorms in the cold front is detected every minute. A striated echo from west to north at 19:25 moves to east with some deformity, and the surface wind wholly blows to northeast. The wind speed is over 20 m s^{-1}, which makes velocity folding area partly, for example, the area around the zonal and the meridional range of -12 and -5 km in panel (3-d). In Figure 2.13, the reflectivity products of the BBR and the C-band radar (non-Doppler) are compared. Panel (a) presents the reflectivity factor of the C-band radar with a range resolution of 500 m and an elevation angle of 0.09°. The C-band radar data adopt ground clutter suppression due to a moving target indicator and do not correct precipitation attenuation. The data over 15 km

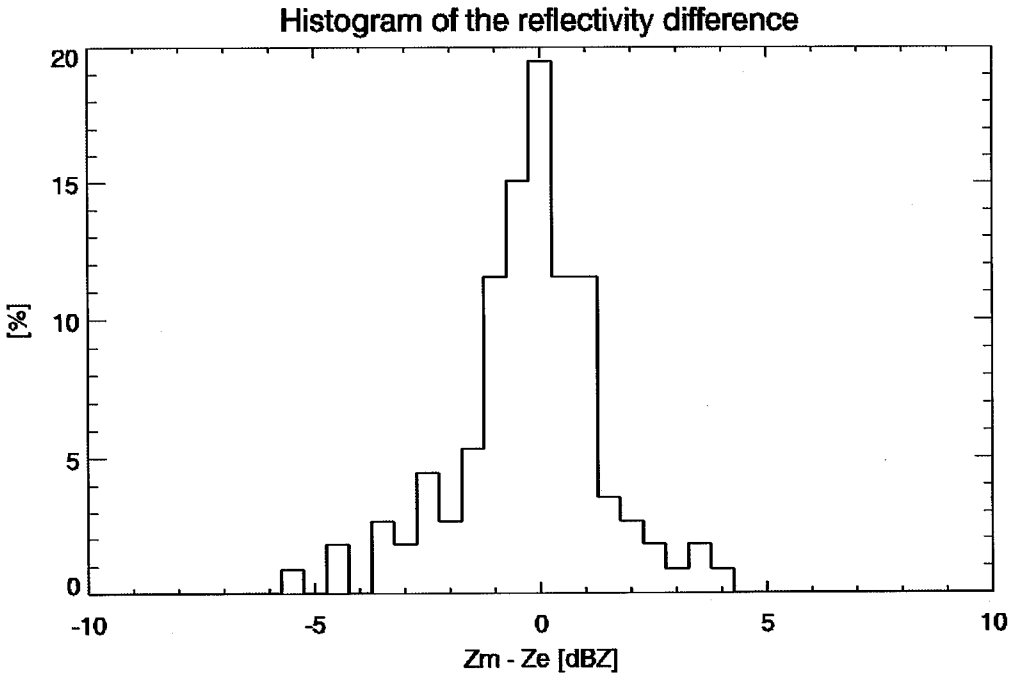

Figure 2.11: Histogram of the reflectivity difference between Z_m (BBR) and Z_e (JWD), except for Z_e under 10 dBZ. The correlation coefficient and the standard deviation are 0.95 and 1.50 dB, respectively.

Table 2.3: Observation characteristics

	Observation I	Observation II
Day and time	15:00 - 19:00, Sep. 14, 2008	16:30 - 20:30, Jan. 22, 2009
Operation mode	Conical	Spiral
Azimuth rotation speed	30.0 RPM	32.7 RPM
Elevation	30°	0 - 90°
Power	10 W (peak)	10 W (peak)
Pulse length	160 μs	139 μs
Inter pulse period	260 μs	239 μs
Pulses / segment	64	64
Waveform	Linear up-chirp	Linear up-chirp
Band width	40 MHz	40 MHz
Weighting window	Raised-cosine window (α=0.1)	Raised-cosine window (α=0.1)

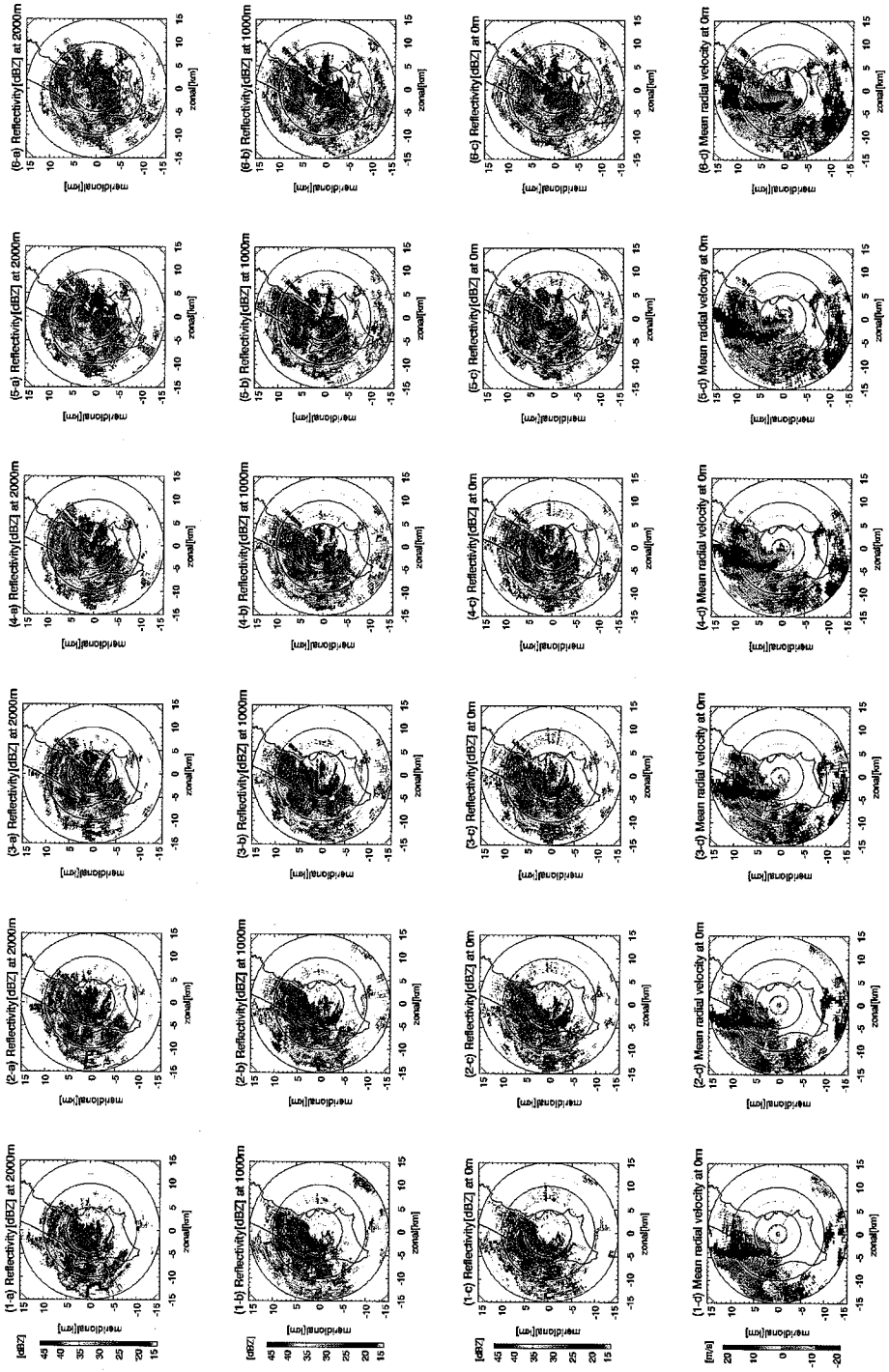

Figure 2.12: CAPPIs in the spiral observation result of reflectivity (dBZ) at 2000, 1000, and 0 m and mean radial velocity (m s^{-1}) at 0 m, from top to bottom, at 19:25, 19:26, 19:27, 19:28, 19:29, and 19:30, from left to right. In the Doppler velocity (bottom panels), positive and negative values indicate velocities toward and against the BBR, respectively.

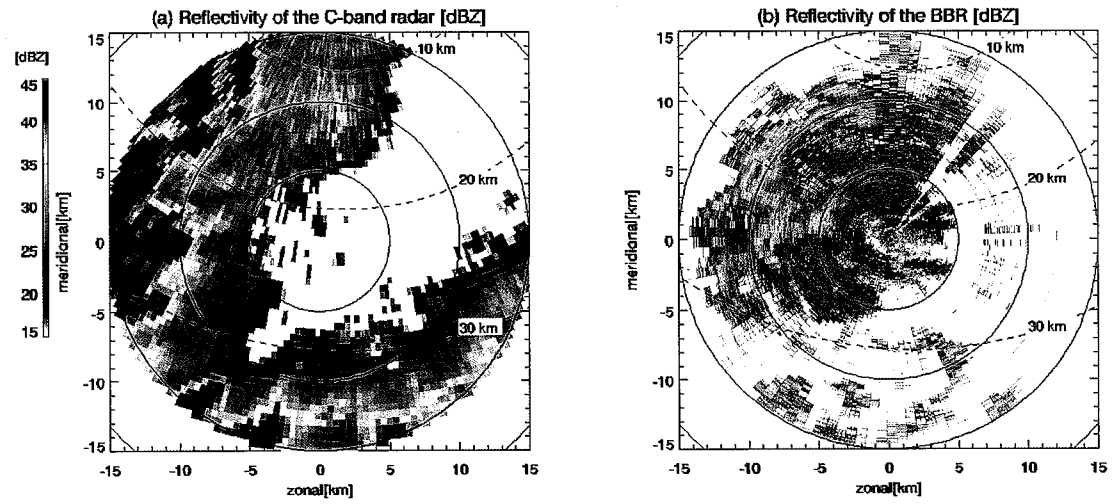

Figure 2.13: Comparison of the C-band radar and the BBR in the lowest scans of reflectivity (dBZ) at 19:28. (a) C-band radar result at an elevation of 0.09° at 19:28. (b) Base scan of the BBR with an elevation from 0° to 3° at 19:28 (a close-up version of panel (4-c) in Figure 2.12). (Dashed lines) 10-, 20-, and 30-km ranges from the C-band radar.

from the BBR are removed to compare them equivalently. The dashed lines indicate the ranges of 10, 20, and 30 km from the C-band radar. That is, the observed volumes of the C-band radar are relatively small at low altitudes since the shown region in Figure 2.13 is in close ranges for the C-band radar. On the other hand, panel (b) presents the reflectivity factor of the BBR base scan at 19:28, which is a close-up version of panel (4-c) in Figure 2.12. In the base scan, the elevation is linearly ascending from 0° to 3° in the circuit. Panel (b) shows the obvious advantage of the fine resolution, such as a small cell around 3 km in zonal range and -7.5 km in meridional range, while panel (a) represents this cell by only few points. Moreover, it is considered that the strong echo around 1 km zonal and 8 km meridional in panel (a) is from ground, since much the same echo appears on the next scan 10 min later. Therefore, this is an example to indicate that it is difficult for a long-range radar to observe at low grazing angles. Panel (b) also shows the disadvantage that the BBR cannot measure reflectivity behind the strong echo accurately and precipitation around the 15-km range is scarcely detected, owing to precipitation attenuation. The range height indicator (RHI) for an azimuth of 128.5° (clockwise, as a benchmark of due south) at 19:30 is shown in Figure 2.14, whose upper and lower panels show the reflectivity and mean radial velocity, respectively. This figure indicates that the BBR detects each small cell separately from a low altitude. In the upper panel, the bright band is clearly seen at about 2.5 km above ground level (AGL), and two strong echoes from 4 to 8 km and from 8 to 12 km ranges are considered as separate convective cells indwelling in the stratiform rain event. In addition, two streaks of precipitation can be resolved in the former cell. The lower panel indicates the advections of the upper and lower layers with different

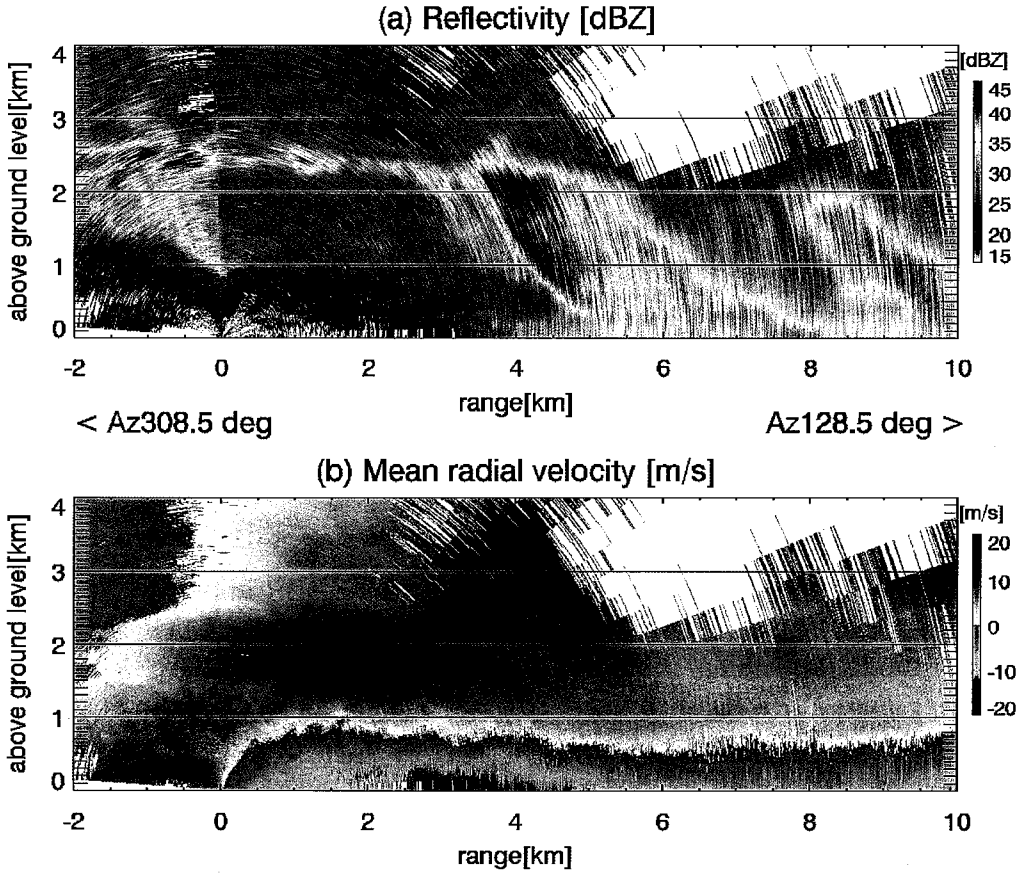

Figure 2.14: RHIs in the spiral observation of reflectivity (dBZ) and mean radial velocity (m s^{-1}) for an azimuth of 128.5° (clockwise, as a benchmark of due south) at 19:30. (a) Reflectivity. (b) Mean radial velocity.

directions. Since the upper wind blows toward the BBR and the lower wind blows against the BBR, the rain drops are horizontally flown by a horizontal distance of about 1.5 km in 2 km AGL. This is an important example representing that the reflectivity products at an altitude of several kilometers do not agree with ground-based instruments. From these figures, it is confirmed that it is important to observe precipitation from a low altitude with highly temporal and spatial resolutions and the BBR has the sufficient capability to analyze 3-D structures of these small-scale phenomena equivalently in terms of time.

As remaining problems, thin concentric echoes from the BBR at 2-, 7-, and 12-km ranges are considered as fractions of the range sidelobes of direct coupling or leakage. Another is that the sensitivity at 15 km is about 30 dBZ. This is caused by the direct coupling of the noise of the transmitter, which is higher than the designed value of 20 dBZ. These problems will be solved in the near-future upgrade.

2.4 Couclusion

In this paper, we have developed the Ku-band BBR, which is a remarkably high-resolution Doppler radar for meteorological application with volume-scanning capability. Due to several characteristics, a bistatic antenna system with low coupling level, low-power transmission, pulse compression with wideband-transmitting pulse, and so on, the BBR can observe precipitation profiles with high range and time resolution from a low altitude.

The conical observation result shows a fairly good agreement with the JWD (Disdromet Inc. RD-80). This means that two uncertain factors of radar observations are suppressed by the high range resolutions and the low minimum detectable range. The rain rate obtained by conventional radars does not necessarily correspond to that of ground-based equipment, such as rain gauges and disdrometers. The nonuniformity distribution of precipitation in a rain scattering volume is considered as a cause of this disagreement. The weather radar equation is constructed under the assumption that the distributed particles completely fill the resolution volume in the same phase at a range bin [2]. Another possible cause is that conventional radars cannot obtain precipitation profiles at low altitude because the radar beam overshoots by an altitude of several kilometers in the range roughly over 150 km due to the Earth's curvature and cannot be transmitted at low grazing angles due to the surrounding landform. In addition, monostatic radars cannot observe in a close range because the receiver must be turned off during transmission. The vertical-pointing observation for precipitation using the radar profilers indicates that the reflectivity profile of precipitation changes by several decibels even under an altitude of 400 m, affected by evaporation, drop, breaking up, and coalescence of raindrops [6].

In the samples of the spiral observation result, it is indicated that the small-scale behaviors in thunderstorm cells are observed by the BBR. Moreover, it remains possible that the future observation and analysis provide us with knowledge about the consequences from the generation to the decay and the prediction for small-scale weather phenomena. In fact, in the work with respect to the other weather phenomena of lightning, Lightning Detection And Ranging system indicates that vertical developments of lightning activity with microscale in thunderstorms with small scale spatially and temporally exist, and these phenomena are possibly followed by tornadoes, downbursts, and so on [22]. The BBR has the potential ability to observe them, and simultaneous use of lightning detection systems, for example, VHF broadband digital interferometer [23], will provide the more elaborate studies. As one of our future works, we are developing the polarimetric BBR now. It is expected that the polarimetric BBR accurately estimates polarimetric products due to the high spatial resolution, and relations between lightning behaviors and hydrometeor classes are clarified. Classification methods for S-, C-, and X-band polarimetric radars are already proposed, and it is considered that these methods can be applied to the polarimetric BBR [24], [25].

However, several problems are remaining. Of course, the devices will be upgraded to suppress the thin concentric echoes and the noise of the transmitter stated in Section 2.2. Then, a correction method for precipitation attenuation will be developed to improve the

observation accuracy of the BBR network. To improve the azimuth resolution, which is worse for the range resolution, the development of an azimuth compression method with high rotation speed will be performed. In addition, more analyses for this thunderstorm, the observation and analysis of other weather phenomena, the development of polarimetric BBR, and the construction of BBR network will be also performed.

Chapter 3

Spectral moment estimation algorithm for the Ku-band broadband radar

3.1 Introduction

In this chapter, an algorithm performed in the latter process is presented in details. The BBR is installed in an urban or rugged mountainous area, in which ground clutter is significant. Reflections from ground clutter are mixed into any range bin and contaminate precipitation signals, and it is necessary to perform an algorithm for ground-clutter suppression as many times as the number of range bins. An algorithm presented in this chapter is designed to suppress ground clutter and estimate Doppler spectral moments with a higher accuracy and a lower computational cost than a conventional method of the moment method [26], even when precipitation echo are overlapped with strong clutter in a spectral domain. Section 3.2 shows a background of ground-clutter suppression and Doppler moment estimation. Section 3.3 shows a methodology of the proposed algorithm. In Section 3.4, performances of the proposed method are assessed by using both simulation models and observational experiments. Section 3.5 summarizes this chapter.

3.2 Background

Performance of a ground based weather radar is adversely affected by ground clutter. In operating at a low grazing angle, a radar detects ground, buildings and trees, etc. by main- or side-lobes, which forces the radar to overestimate power of a weather target by several decibels and misestimates mean velocity and spectral width especially in low range. The BBR is more affected by ground clutter than conventional radars because its observable range is very low and the BBR is occasionally installed in an urban or rugged mountainous area to fill gaps of the observational area which conventional radars have especially in low altitudes.

In the past, weather radars adopted a fixed notch-width infinite impulse response (IIR) clutter filter followed by a time domain autocorrelation processing (pulse-pair process-

ing) [26] for real-time observation. This approach requires very short processing time per range bin, and is suitable for real-time signal processing. However, when a radar detects target signals which have velocities near 0 m s^{-1}, an IIR filter seriously cut the signals together with the overlapped clutter signal. In using this approach, furthermore, operators must manually select a filter that is adaptive for the clutter, since clutter power and width changes for circumstances around radars. Other systems employed a frequency domain process commonly called a spectral processing [26]. Spectral approaches can adequately filter ground clutter by searching and determining a clutter region in a frequency domain. On the other hand, one of disadvantages of a spectral processing is a finite spectral resolution. The spectral resolution is constrained by an FFT that is implemented only on condition that the number of point is a power of 2 (e.g. 16, 32, 64, 128). In addition, a spectral leakage of ground clutter signals caused by finite sample length severely contaminates Doppler spectrum, particularly with highly clutter-to-signal ratio (CSR). To suppress effects of the spectral leakage of clutter signals, a window weighting function is applied to I and Q values. However, a weighting window broadens spectral width and causes an overestimation in spectral width and a reduction of radar sensitivity.

Recent computational developments allowed for use of advanced radar signal methods, and many techniques with high estimate accuracy have been proposed. These techniques, however, include several procedures, like an inversion of a large matrix, which needs high computational cost. Gaussian Model Adaptive Processing (GMAP) [27] and Parametric Time domain Model (PTM) [28] are able to detect Doppler spectrum information with very high accuracy. However, they are not suitable for its iterative implementation in a short time due to including costly processes. The BBR is a remarkable high resolution radar that calculates 64-points FFT in 2^{13} (8192) range bins within 15 ms in one direction. Therefore, it is almost impossible to adopt these techniques in real-time observation. And a simple algorithm with a high estimate accuracy are necessary for the BBR.

3.3 Methodology

Our approach makes several assumptions about clutter, weather and noise as follows.

- Spectral width of precipitation signal is greater than that of clutter.
- Doppler spectrum consists of a single weather target, ground clutter and noise.
- Width of the clutter signal is approximately known. A clutter width is able to be predicted by an angular velocity, a wave length and so on of the BBR or be measured preliminarily. The assumed clutter spectral width is used to determine how many interior clutter points are removed.
- A shape of the clutter is approximately a Gaussian. This shape is used to calculate how many spectral points are removed.

- A shape of precipitation is approximately a Gaussian. This shape is used to reconstruct precipitation signals.

The proposed technique applies a rectangular weighting function that leads to the lowest variance estimates of power, mean velocity, and spectral width. A more aggressive window weighting such as Hamming or Blackman broadens spectral width and reduces a spectral peak of precipitation, resulting to deteriorate radar sensitivity because a window weighting means a cross correlation between raw spectrum and the window function in a frequency domain. A clutter region is analytically determined to cancel ground clutter components by assuming a Gaussian distribution for clutter. Precipitation signals are also analytically determined in a similar way. This method assumes that shapes of ground clutter and precipitation are Gaussian as GMAP and PTM. By excluding all costly procedures, a processing time is significantly reduced. Figure 3.1 shows an overview of the proposed method. Steps to implement this technique are summarized below.

– Step 1: Elimination and interpolation for clutter points

  It is known that ground clutter appears around a velocity of 0 m s^{-1} and a shape of ground clutter is approximately Gaussian changing its power and width for circumstances of each radar sites [29]. In order to determine clutter points, a Gaussian, which is not shifted (the peak is positioned in 0 m s^{-1}), normalized by the peak value (the peak value equals to 1), and has a specified width, is prepared. The Gaussian multiplied by a value of the central point of Doppler spectrum (the DC component value) is named "the Gaussian clutter" here. Then, points between intersections of the Gaussian clutter and Doppler spectrum are removed and interpolated based on an Hermite interpolation [30] which restores a spectral shape of precipitation in case of the precipitation components are seriously cut in the clutter elimination. The BBR observes ground clutter with the width of about 0.25 m s^{-1} in a fixed pointing mode. Clutter is adequately suppressed when we set a width of the clutter Gaussian to 0.28 m s^{-1}.

– Step 2: Determination of noise level

  Spectral noise power can be measured preliminarily. However, noise power will differ from measured noise power for strong clutter targets. The clutter target or range sidelobes of the clutter, caused in a pulse compression radar, increases the spectral noise level in all frequency ranges because a small amount of phase noise affects more and window sidelobes can not be neglected in this case.

  After step 1, the Doppler spectrum approximately consists of precipitation and noise. First, the peak power point is searched. Components around the peak power point are precipitation and else ones are noise. In this algorithm, the noise table which indicates the noise components is prepared and the noise level is determined by averaging the points indicated by the table. The table consists of components a velocity away from the precipitation peak. The number of noise components is specified not to be contaminated by precipitation. In our Doppler estimation which

calculates a 64-point FFT with a Nyquist velocity of about 20 m s^{-1}, the number of noise components is 4.

– Step 3: Estimation of Doppler spectral moments

Using the clutter suppressed spectrum, the first three spectral moments are estimated in this step. Several components (the number is specified) around the peak power point, which is searched in Step 2, are chosen. After the noise power calculated in Step 2 is eliminated from each component, the first moment of them is calculated as mean velocity of precipitation. The number of the components used in the first moment calculation is set 9 of a 64-FFT points as a result of trade-off between a calculation cost and an estimate accuracy. Power and spectral width are calculated with use of a Gaussian function expressed as

$$S(v) = a\exp\left[-\frac{1}{2}\left(\frac{v-b}{c}\right)^2\right], \tag{3.1}$$

where, $S(v)$ is power spectral density, v is Doppler velocity and a, b, and c are a peak value, a position of the peak and width of Gaussian, respectively. The peak power (from which noise power is eliminated) is substituted for a. Then powers of two points positioned about a specified velocity away from mean velocity is assigned to $S(v)$ and the specified velocity is assigned to $(v-b)$ to calculate the spectral width of precipitation, c. Finally, the power of precipitation, P, is calculated from an integral of a Gaussian function as

$$P = \int_{-\infty}^{\infty} S(v)dv = ac\sqrt{2\pi}. \tag{3.2}$$

When the specified velocity is set to a high value, the points at the velocity away from the peak position are often noise components. When the velocity is a small value, on the other hand, the variance of calculated c is increased. The observed spectral width of precipitation is mostly from 1 to 2 m s^{-1} on the BBR, because of its range resolution of several meters and beam width of 3°. Therefore, we set the specified velocity to about 1.8 m s^{-1} (3 points of 64-FFT points with the Nyquist velocity of 20 m s^{-1}). When one of the using components are folded by aliasing, this algorithm corrects only the components to the side of the peak point.

3.4 Result of implementation

3.4.1 Simulation

To evaluate performances of the proposed method, radar signal simulations were carried out. A simulated signal for the evaluation is described as following Gaussian form.

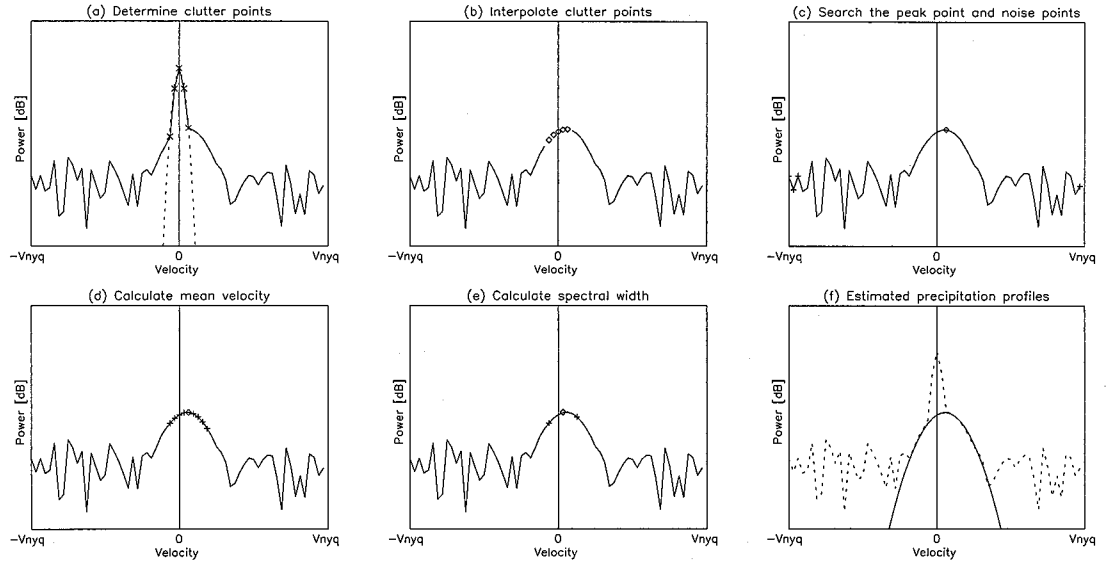

Figure 3.1: Overview of the proposed method (a) Determination of clutter points: Solid line is power spectral density, dot line is an estimated Gaussian clutter, and x marks are classified as clutter points under the Gaussian clutter. (b) Interpolation at clutter points: Solid line is power spectral density, and diamond marks are the points restored by an Helmite interpolation. (c) Search for a peak point and noise points: Solid line is power spectral density which consists of precipitation and noise. Diamond mark is the peak point and plus signs are noise points on a noise table of the proposed method. A spectral noise power is determined by averaging the noise points. (d) Calculation of mean velocity: A diamond mark is the peak point and plus signs are the components neighboring the peak point. These components eliminated noise power are used to calculate first moment as a mean velocity. (e) Calculation of spectral width: A diamond mark indicates the mean velocity calculated in (d) and the peak power eliminated the noise level. Two plus signs are components positioned a specified velocity away from the mean velocity. Diamond mark is used as a parameter of the peak of precipitation Gaussian and the mean power of two plus signs and the specified velocity are used to calculate spectral width. (f) Estimation of precipitation profiles: Solid line is estimated precipitation Gaussian and dot line is power spectral density before applying this method.

The Doppler spectrum, $M(v)$, can be written as

$$M(v) = \sum_{N}^{i=1} M_i(v) + \sigma_n^2, \tag{3.3}$$

where

$$M_i(v) = \frac{P_i}{\sqrt{2\pi}\sigma_{vi}} \exp\left[-\frac{1}{2}\left(\frac{v-\overline{v_i}}{\sigma_{vi}}\right)^2\right]. \tag{3.4}$$

Here σ_n^2 represents a noise spectral power density. Now, the number of signal, $N(=2)$, denotes precipitation and ground clutter. The BBR is not affected by Bragg scattering from air motions. The other parameters used for the simulations are given in Table 3.1. A CSR of 50 dB indicates a differential scattering cross section of ground return is 41.5 dB under a condition that the radar reflectivity factor from rainfall is 20 dBZ. Figure 3.2 shows filtering performances of this method. Designed mean velocities normalized by the Nyquist velocity and spectral width of precipitation model are, respectively, indicated by the horizontal axis and line types in all panels. The upper panels show bias errors of estimated powers, mean velocities and spectral widths of precipitation and the lower panels show standard deviations of them. A bias error and a standard deviation are calculated using 8000 simulation models with different additive white Gaussian noise (AWGN) patterns in each parameter to converge them sufficiently. For comparison, performances of a traditional method based on the moment method is also shown in Figure 3.3. The traditional method discards 5 central points of the Doppler spectrum and interpolates them linearly for clutter suppression. Then the first three moments are calculated using points over a fixed threshold level of 10 times a designed spectral noise power for noise suppression. A high threshold level deteriorates radar sensitivity instead of high estimate accuracy because it often eliminates not only noise components but also precipitation components. The moment method and these options are considered to be able to calculate on the BBR real-time observation for computational efficiency.

Panel (a) in Figure 3.2 and 3.3 show that the proposed method is less affected by ground clutter. While absolute values of bias error of the proposed method are 1.75 dB in the spectral width of 1 m s^{-1} and 0.32 dB in 2 m s^{-1} at a maximum, those of the traditional method are, respectively, 7.28 dB and 1.35 dB, which are about 4 times worse than the proposed method. Each Panel (a) and (d) shows bias errors and standard deviations of the proposed method are nearly the same as the traditional method in low spectral widths of 1 and 2 m s^{-1}. Though those are inferior in the higher spectral widths but under 0.70 dB in bias error and 0.35 dB in standard deviation. In Panel (b) and (c), the proposed method shows better performances than the traditional method in all the velocities. In Panel (b), absolute values of the peaks in a low normalized velocity are improved 1.5-3 times in each spectral width. In addition, while the traditional method is adversely affected by aliasing in the normalized velocity over 0.68, the proposed method is less affected than 0.84. In Panel (c), the proposed method is superior in all the velocities and the traditional method is highly affected by aliasing in high normalized velocities as Panel (b). Panel (c) in Figure 3.2 shows high errors appearing in spots especially in a spectral width of 1 m s^{-1}. This is because the proposed method overestimates spectral width when the peak of Gaussian distribution in precipitation is not positioned at a discrete velocity point of Doppler spectrum. It is shown in Panel (a) of Figure 3.2 that these errors of the proposed method affect its power estimation. Panel (e) also shows the proposed method is unaffected by ground clutter and nearly the same as the traditional method in the low spectral widths of 1 and 2 m s^{-1}. A difference of the aliasing effects to these two methods appears in high normalized velocities over 0.6. While precipitation signals divided and positioned to both side edges of Doppler spectrum by aliasing are estimated to around 0 m

Table 3.1: Simulation specification

Frequency	15.75 GHz
Pulse repetition frequency	5 kHz
FFT point	64
Signal to noise ratio	8 dB
Clutter to signal ratio	50 dB
Spectral width of precipitation	1, 2, 3, 4 m s^{-1}
Spectral width of clutter	0.25 m s^{-1}

s^{-1} in the moment method, the proposed method estimates near the peak point, whether or not precipitation signals are divided. Panel (f) also shows that the proposed method is better in the lower spectral widths because parameters of this algorithm are set for spectral width of 1-2 m s^{-1} as stated in Step 3. In the higher spectral widths, a standard deviation are about 0.5 m s^{-1} at a maximum. In a higher normalized velocity, the traditional method is more affected by noise components over a threshold level. Standard deviations of the moment method in high normalized velocities over 0.8 are low because estimated mean velocities are around 0 m/s by aliasing.

These simulation results indicate that the performance of the proposed method is superior to the traditional method in narrow spectral widths below 2 m s^{-1}. High range resolution radars obtain small values of spectral width because the observation data are less affected by shear and so on. Therefore, it can be said that this method suits for high range resolution radars.

3.4.2 Computational efficiency

Computational effciency of an algorithm depends on each system structures, parts, and tips, and it is difficult to equally compare them. To evaluate the computational efficiency of this algorithm, the step number of this algorithm on our signal processing system using digital signal processors (DSPs) is presented here. For comparison, the step number of the traditional method is also shown. Table 3.2 shows specifications of a DSP used in our system and the step numbers of two algorithms on our system. A step number of this algorithm is much less than that of the traditional method, denoting that this algorithm has over two times higher speed than another, except for internal caches of the processor. Six DSPs are parallely operated on our system and this algorithm has enough simplicity to be processed within 2 μs at one time. Since, on the BBR, one direction comprises 8192 range bins in the range of 15 km, this algorithm is calculated at one direction within 15 ms.

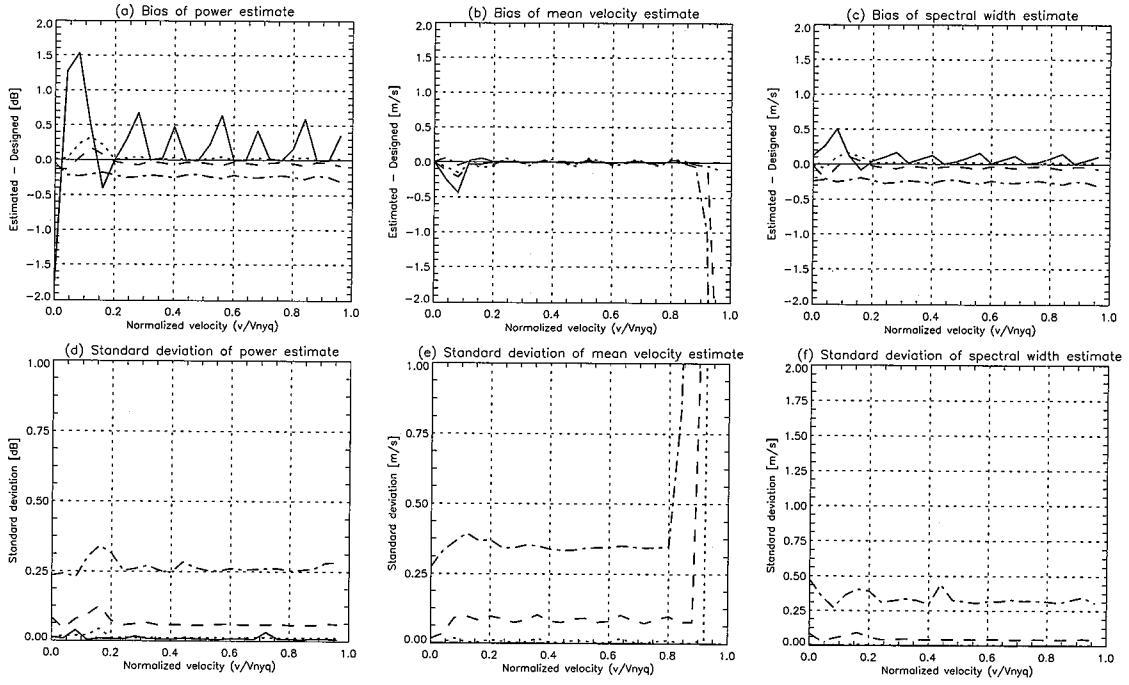

Figure 3.2: Statistical performance of the proposed method: Solid is 1 m s^{-1}, Dot is 2 m s^{-1}, Dash is 3 m s^{-1}, Dash dot is 4 m s^{-1} of spectral width of signal: (a) Bias of power estimate, (b) Bias of mean velocity estimate, (c) Bias of spectral width estimate, (d) Standard deviation of power estimate, (e) Standard deviation of mean velocity estimate, (f) Standard deviation of spectral width estimate.

Table 3.2: Simulation specification

DSP	
Maker	Texas Instrument
Type	TMS320C6713BZDP300
Frequency	300 MHz
Step number (64 points)	
FFT	2038
The proposed method	3865
The moment method	8091

3.4.3 An example of implementation on the BBR

The proposed method was applied to precipitation data observed by the BBR to test performances. An operation characteristics of the observation are given in Table 3.3. Fig-

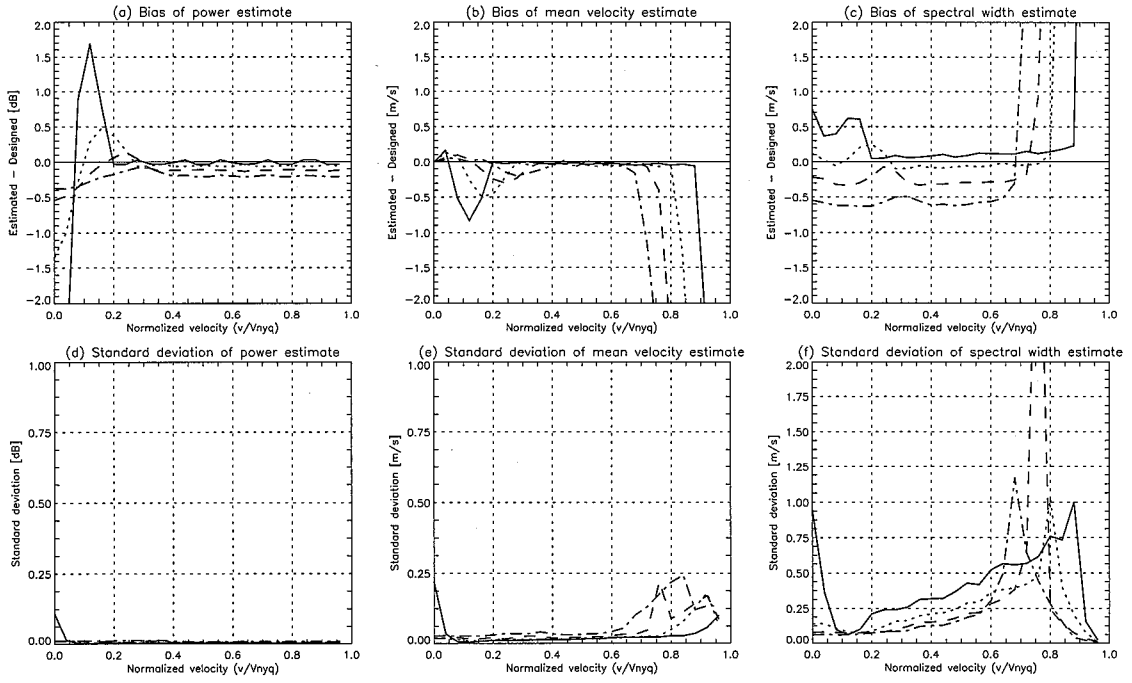

Figure 3.3: Statistical performance of the moment method: Solid is 1 m s^{-1}, Dot is 2 m s^{-1}, Dash is 3 m s^{-1}, Dash dot is 4 m s^{-1} of spectral width of signal: (a) Bias of power estimate, (b) Bias of mean velocity estimate, (c) Bias of spectral width estimate, (d) Standard deviation of power estimate, (e) Standard deviation of mean velocity estimate, (f) Standard deviation of spectral width estimate.

ure 3.4 shows an example of Doppler spectrum at a range of 198 m. It is clear that all the susceptible ground clutter is removed and the precipitation signal is correctly identified. A power of the proposed method is -34.49 dB which is 2.32 dB larger than that of the moment method because the Helmite interpolation restores the spectral shape of precipitation. Because the linear interpolation tends to underestimate the power, a mean velocity and a spectral width of the moment method are overestimated by 0.64 m s^{-1} and 0.57 m s^{-1} respectively in this example. However, the BBR is occasionally operated in a spiral mode to observe 3-D structures of rainfall, and its accuracy of this method is deteriorated in high elevation angles in which a spectral shape of precipitation is not Gaussian. In such a case, non-parametric methods which do not assume a spectral shape are efficient.

3.5 Conclusion

This chapter presents a new method which suppresses ground clutter and estimates spectral moments of precipitation signals in real-time. Due to the simplicity of this algorithm, Doppler spectrum information is estimated in a very short processing time. There-

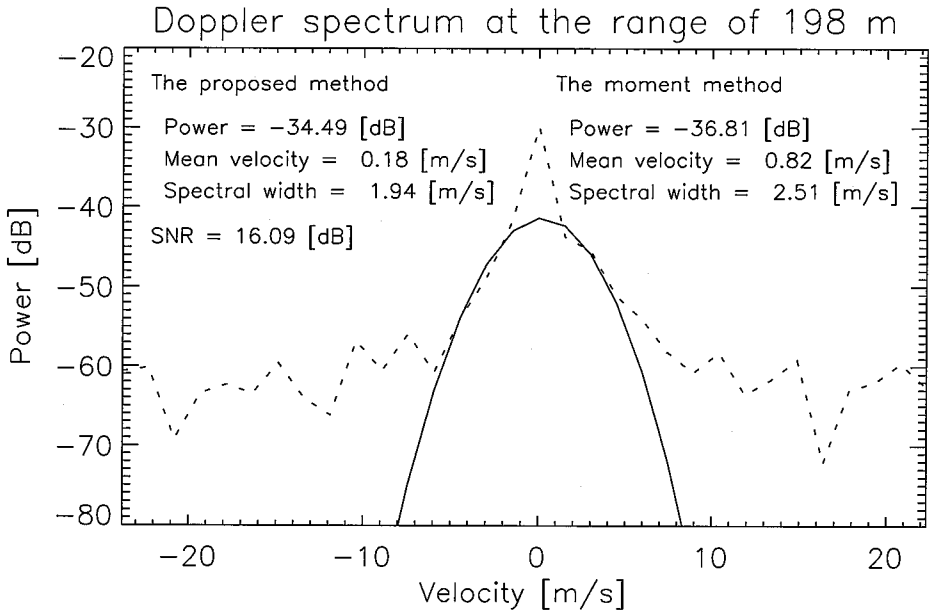

Figure 3.4: An example of implementation on the BBR: Solid line is estimated precipitation Gaussian and dot line is power spectral density before applying this method. A power, a mean velocity and a spectral width estimated this method is -34.49 dB, 0.18 m s^{-1} and 1.94 m s^{-1}, respectively. Those of the moment method are -36.81 dB, 0.82 m s^{-1} and 2.51 m s^{-1}. A SNR of 16.09 dB is calculated from the power and the spectral noise power estimated by this method.

Table 3.3: Operation characteristics

Day	2007/12/28
Place	Osaka university, Japan
Pulse length	128 μs
Pulse repetition frequency	2.5 kHz
Pulses / sequence	32
Power	500 mW
Frequency	15.71 - 15.79 GHz
Band width	80 MHz
Antenna elevation	30°

fore, this method is optimal for real-time observation on a very high resolution radar, like the BBR. The performance are superior to the traditional method and estimate accuracies are higher in a narrow spectral width below 2 m s^{-1}. Computational efficiency of this

algorithm also is superior as low processing time within 2 μs at one time on our DSP system. The significant feature of this method is that the compact algorithm can respond to many critical matters, for example, strong clutter, divided precipitation spectrum, and so on, and accurately estimate the values of total power, mean velocity and spectral width of precipitation signals.

Chapter 4

Vertical structure of precipitaiton in lower atmospheric boundary layer

4.1 Introduction

A scientific topic, vertical structure of DSD in lower atmospheric boundary layer (below an altitude of 300 m), is presented in this chapter. This topic is derived by a minimum detectable range of 50 m and a high spatial resolution of several meters, which are significant characteristics of the BBR. In this study, DSD are measured with two co-located instruments, the BBR and a 2 dimensional video disdrometer (2DVD) in Osaka, Japan. The DSD profiles that are retrieved from the vertical Doppler spectrum (VDS) of the BBR in the lower ABL (50 m through 300 m) are compared to the DSD estimated by the 2DVD. Using these instruments, we discuss the differences of vertical structures of the DSD in the lower ABL between stratiform and convective rain events. Section 4.2 describes equipments used in this study. Section 4.3 presents a method for DSD retrieval. Section 4.4 shows analysis results of vertical structures of DSD in a stratiform and convective event, separately. Section 4.5 summarizes this chapter.

4.2 Equipments and observation characteristics

We observed vertical precipitation profiles using a prototype BBR observing a fixed direction using a bistatic antenna system [31]. The antennas of the prototype BBR were upgraded to Luneburg lenses which achieve a 3-dB beam width of 3°. The observational characteristics of the BBR are shown in Table 4.1. The transmitting waveform is a linear up-chirped and raised-cosine windowed ($a = 0.3$) pulse of 128 ms duration and 80 MHz bandwidth, which ideally achieves 3-dB range resolution of about 6 m. Since the digital sampling frequencies (250 or 400 MHz) have smaller wavelengths than the range resolution in this observation, the BBR products are averaged every 5 m. The VDS is measured every 3 s by the BBR outputs from a sequence of sixty-four pulses (there is a data-offload time of about 2.8 s). The 2DVD that is used for validation is an optical sensor that detects

Table 4.1: Observation characteristics

	Observation I	Observation II
Center frequency	15.75 GHz	15.75 GHz
Band width	80 MHz	80 MHz
Operation mode	Vertical pointing	Vertical pointing
Power	2 W (peak value)	2 W (peak value)
Pulse length	128 μs	128 μs
Modulation	Linear up-chirp	Linear up-chirp
Weighting window	Raised-cosine window ($\alpha = 0.3$)	Raised-cosine window ($\alpha = 0.3$)
Sampling frequenct	400 MHz	250 MHz
Inter pulse period	200 μs	200 μs
Pulse number / sequence	64 pulses	64 pulses
Sequence interval	3 s	3 s
Nyquist velocity	23.79 m s^{-1}	23.79 m s^{-1}
Doppler velocity resolution	0.37 m s^{-1}	0.37 m s^{-1}
Day and time	22:00, May 28, 2008 through 6:00, May 29, 2008	16:50 - 17:50, Sept. 5, 2008 and 8:50 - 9:30, Sept. 26, 2008
Place	Osaka university, Suita	Osaka university, Suita
Remarks	Stratiform rain event	Convective rain event

each rain drop [15], and it was collocated a distance 15 m horizontally and 25 m below the BBR. The outputs of the 2DVD are accumulated and averaged over 1 min intervals to ensure that a statistically significant number of rain drops are sampled. Correspondingly, the BBR output is also averaged over 1 min intervals (20 values are averaged because the sequence interval is 3 s).

Two separate events were observed, one stratiform and one convective. The observational periods for the stratiform and convective events were 480 and 100 minutes, respectively. The two measurements are time synchronization through cross-correlation analysis. The reflectivity factors calculated from the BBR at an altitude of 50 m are compared with the 2DVD measurement, and the 2DVD data are time-shifted to the BBR to give the highest cross-correlation coefficient. The reflectivity factor of the BBR is then calibrated by the mean difference between reflectivity factors of the BBR at the 50 m altitude and 2DVD.

4.3 Retrieval for raindrop size distribution

In this section we describe the methodology of DSD retrieval employed in this study. The DSD retrieval consists of 3 steps; 1) the conversion of VDS to DSD, 2) the fitting to a Gamma DSD, and 3) the correction for precipitation attenuation. The VDS near velocities of 0 m s^{-1}, and hence measurement of small-diameter raindrops, is contaminated by DC components in the instrumentation electronics and by motionless targets, so only number densities over 0.9 mm are estimated in Step 1. In Step 2, the DSD estimated in Step 1 is fitted to a Gamma DSD to estimate number densities of precipitation under 0.9 mm in diameter. Step 3 corrects precipitation attenuation for a VDS at a given range bin using the DSDs of all the bins behind. Steps 2 and 3 are performed iteratively and deterministically beginning with the closest bin (50 m) in which no precipitation attenuation is assumed. The other assumptions contained in this study are described below.

– Step 1: Conversion of VDS to DSD

  Assuming that background winds are neglected and that all the raindrops in the radar resolution volumes fall at terminal velocity, the relation between a VDS and DSD is approximated as

$$S(v_t)dv_t \approx \frac{\lambda^4}{\pi^5|K|^2}\sigma_b(D)N(D)dD, \tag{4.1}$$

  where v_t is the terminal fall velocity (m s^{-1}), $S(v_t)$ is the VDS (mm^6 m^{-3} (m $s^{-1})^{-1}$), λ is the wavelength (mm) of a transmitting wave, σ_b is the Mie back scattering cross section (mm^2) [13], and $N(D)$ is the DSD (m^{-3} mm^{-1}). Also, the diameter of a raindrop D (mm) is empirically related to v_t as reported by [32],

$$v_t(D) = 9.65 - 10.3\exp(-0.6D). \tag{4.2}$$

  Equation 4.2 precludes terminal velocities over 9.65 m s^{-1}. In the previous works using wind profilers which receives both back scattering from raindrops and Bragg scattering from air (containing vertical air motions and turbulences) in a VDS [6], several superior methods to estimate DSD from a VDS that eliminate background winds have been proposed [33], [34]. On the other hand, air motions are not detected in the BBR. In this study, turbulences are simply neglected due to the remarkable spatial resolution of the BBR (the beam width at 300 m is about 15 m). Vertical air motions are neglected because low altitudes (under 300 m) are being studied, although this may introduce errors into the calculations. However, the boundary condition of vertical air speed is 0 m s^{-1} at ground and the mean vertical velocity of air motions over about 1.5 km is 0.5 m s^{-1} [36], so the vertical air motion in the lower ABL is estimated to be about 0.1 m s^{-1}, which yields a maximum error in number density of 1.5 dB. Strong downdrafts, such as microbursts, might break this assumption, so it is necessary to eliminate events in which these

occur. Strong downdrafts occur more often in convective than stratiform events. We have sufficiently confirmed that the data analyzed in this study do not contain strong downbursts by examining the time-height cross sections of reflectivity and mean vertical velocity (not presented here).

– Step 2: Fitting to Gamma DSD

A 3° beam width will have some spectral broadening due to turbulence and horizontal wind across the beam, depending on Doppler spectrum resolution. A power of DC component leaks into adjacent bins of low velocities, which correspond to diameters under 0.9 mm in DSD. In Step 2, the DSD that were estimated in Step 1 are fitted to the Gamma DSD to estimate the number densities of precipitation under 0.9 mm diameter. The Gamma DSD [37] is expressed as

$$N(D) = N_0 D^{\mu} \exp(-\Lambda D) \quad (0 \leq D \leq D_{max}), \tag{4.3}$$

where the exponent μ can be any positive or negative value, N_0 and Λ are the coefficients of the units of (m^{-3} $mm^{-1-\mu}$) and (mm^{-1}), respectively, and D_{max} is the maximum drop diameter (mm). Since the DSD from a VDS have an insufficient number of samples for a good fit, μ is sensitive to fluctuations in VDS. Therefore, we employ an empirical and statistical relationship between N_0 and μ [37] [38] shown in Equation 4.4,

$$N_0 = 6 \times 10^3 \exp(0.9\mu). \tag{4.4}$$

Considering these characteristics, the optimal parameters of the Gamma DSD, N_0, μ, and Λ, are determined by least squares error minimization on a logarithmic scale, that is, by minimizing the cost function

$$J = \sum_i [\ln(N_{BBR}(D_i)) - \ln(N_{GAMMA}(D_i))]^2, \tag{4.5}$$

where $N_{BBR}(D)$ and $N_{GAMMA}(D)$ are the DSDs in Equations 4.1 and 4.3, respectively. In this fit, D_i is above 0.9 mm. Figure 4.1 shows the DSD that are estimated from the BBR along with the 2DVD, and that there is good agreement between the two for raindrops of diameters greater than 1 mm. The 2DVD underestimates the number density of raindrops smaller diameters, especially less than 0.75 mm because the smaller raindrop is frequently obscured by larger raindrops at the optical wavelengths used by the 2DVD measurement.

– Step 3: Correction for Precipitation Attenuation

Although precipitation attenuation does not significantly affect the measurement of precipitation profiles with VDS at the close ranges of focus in this paper, an effort

is made to apply a precipitation attenuation correction for accurate validation. The attenuation coefficient k (dB km^{-1}) can be calculated from the DSD as

$$k = 4.343 \times 10^{-3} \int \sigma_e(D) N(D) dD, \tag{4.6}$$

where σ_e is the Mie extinction cross section (mm^2) [13]. The reflectivity factor at a given range bin is corrected deterministically using the total attenuation of all preceding range bins. This correction method is the same as a recursive approach of Hitschfeld-Bordan (HB) solution (elaborated in the next chapter), except that k is calculated from $N(D)$ in each range bin as Equation 4.6 instead of using a k-Z_e relation. Though the deterministic approaches for precipitation attenuation correction are unstable over long ranges, it is known that they are more stable at the closer ranges of focus here [39].

Here, a simple method of correction for precipitation used only in the study of this chapter is described. A correction method with higher accuracy performed in operations of the BBR network is presented in Section 5.3.

4.4 Observation results

4.4.1 Varidation of retrieval for raindrop size distribution

Figure 4.2 shows the comparison of DSDs from the BBR and 2DVD during a period of 60 minutes. The left-side panels (a-1 through 3) and the right-side panels (b-1 through 3) are for the stratiform and convective events, respectively. The top panels (a-1 and b-1) and the middle panels (a-2 and b-2) are, respectively, the results from the BBR and 2DVD, and the colors represent number densities in m^{-3} mm^{-1} from -20 to 40 dB. The bottom panels (a-3 and b-3) indicate the correlation coefficient of both instruments in each minute. The time averages of the correlation coefficients are 0.74 and 0.78 in the stratiform and convective events, respectively. These correlation coefficients are calculated on a logarithmic scale for all diameters from 0 to 10 mm in diameter every 0.25 mm. If raindrops of diameter less than 0.75 mm are excluded, the correlation coefficients increase to 0.98 and 0.96 for stratiform and convective events, respectively. Thus, the two instruments perform well and are in good agreement for raindrops of diameter greater than 0.75 mm for the stratiform and convective events.

4.4.2 Vertical structure of precipitation

Figure 4.3 shows the vertical structures of the time-averaged (over 60 min) DSD for the stratiform and convective events in the left-side panels (a-1 and 2) and the right-side panels (b-1 and 2), respectively. In the stratiform event (a-1), the DSD do not show significant change below an altitude of 300 m, indicating that the growth and breakup

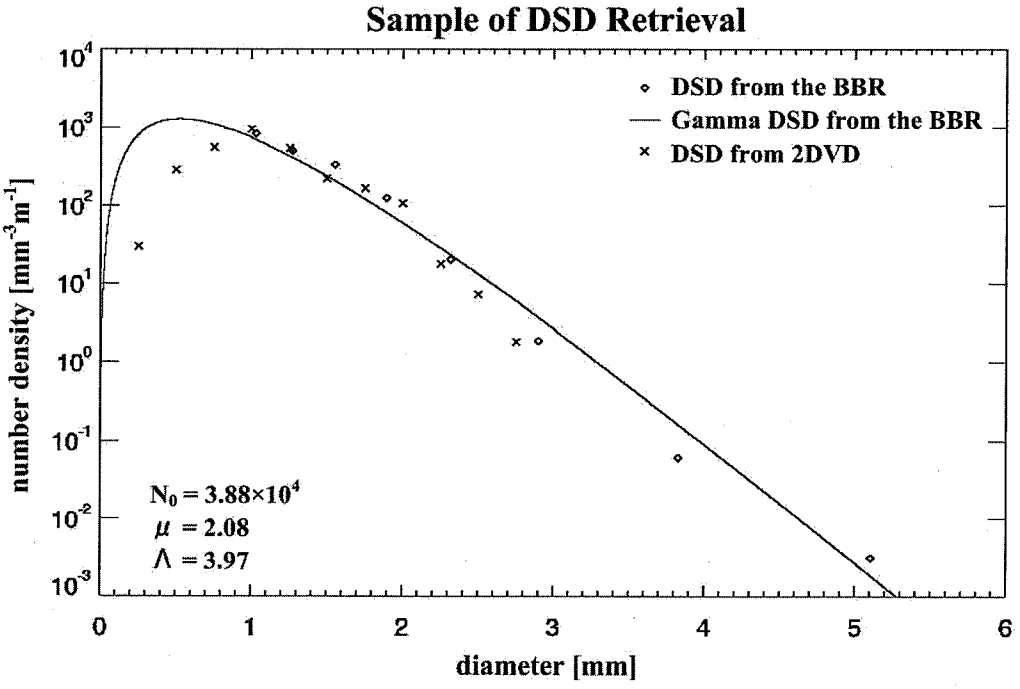

Figure 4.1: An example of DSD retrieval from the BBR. Diamond marks indicate DSD retrieved from the VDS of the BBR. Solid line is the result of fitting BBR DSD to Gamma distribution whose parameters in this case are also shown on the bottom-left corner in the panel. Cross marks indicate DSD estimated by 2DVD.

processes of raindrops are balanced to the equilibrium condition for the stratiform event in the lower ABL. In the convective event (b-1) the raindrops over a 0.9 mm diameter (which are directly retrieved) grow in size as altitude decreases. Since larger raindrops generally fall at faster terminal velocities, the lower region becomes denser even below 300 m altitude in the convective event. The bottom panels (a-2 and b-2) shows the differences in number densities (in dB) from 300 m to lower altitudes (200, 100 and 50 m) for each event. The number density differences are probably not significant for precipitation of diameter less than 0.2 mm(because the density estimation may be inaccurate, see Step 1 in Section 4.3), or greater than 4mm in the stratiform event (due to the relatively low number density). For the stratiform event (a-2), the most considerable shift is about -1.4 dB (a factor of 0.77) at 2.2 mm in the 50 m and 300 m difference. In the convective event, growth processes generate larger raindrops over 0.9 mm in diameter as stated above, especially for precipitation over 2 mm in diameter. In the convective event, the differences of the number densities between 100 and 300 m, and between 50 and 300 m, respectively, have the maximum values of 2.9 dB at 4.5 mm and 3.2 dB at 4.1 mm. While the number densities from 3 to 5 mm in diameter approximately double from 300 to 100 m in altitude, there are no significant changes in DSD under 100 m altitude.

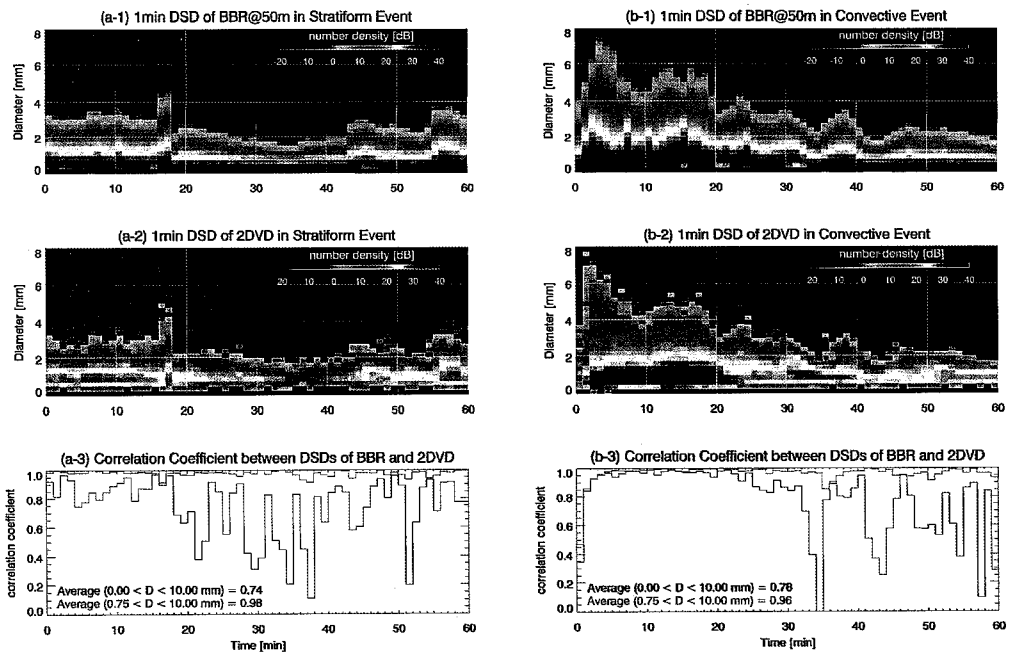

Figure 4.2: Comparison of DSDs from the BBR at a 50 m altitude and 2DVD. (top) Time series of DSD retrieved from the BBR. (middle) That from 2DVD. The colors represent number density (m^{-3} mm^{-1}) in dB. (bottom) Correlation coefficient between them in a logarithmic scale. The black lines are the correlation coefficient calculated with the DSD from BBR between 0 and 10 mm in diameter and the red lines are between 0.75 and 10 mm in diameter. (left and right) Results of the stratiform and convective event, respectively.

4.5 Conclusion

We have shown that the BBR can estimate DSDs accurately for precipitation of diameter greater than 0.75 mm. The measurement of DSD from the BBR is in excellent agreement with that of the collocated 2DVD, indicating that the BBR can effectively measure precipitation profiles in the lower ABL.We used the BBR measurements of DSD to study the precipitation profiles in the lower ABL under 300 m in a stratiform and a convective event. The vertical precipitation profile in the ABL indicates that there is no significant change in the DSD in the stratiform event, but in the convective event the growth of DSD from 300 m to 100 m altitude is clearly shown. Table 4.2 indicates that in the Z-R relation, the coefficient increases with altitude while the exponent almost never changes in the convective event. The changes in the Z-R relation amount to a maximum bias error of 2 percent to the estimated rainfall rate (although higher errors can occur at higher altitude). In the lower ABL, Z-R relation does not change, but Z and R increase as raindrops approach the ground. Thus, conventional radars may get the right Z-R relationship, but they cannot measure the increase in rainfall rate.

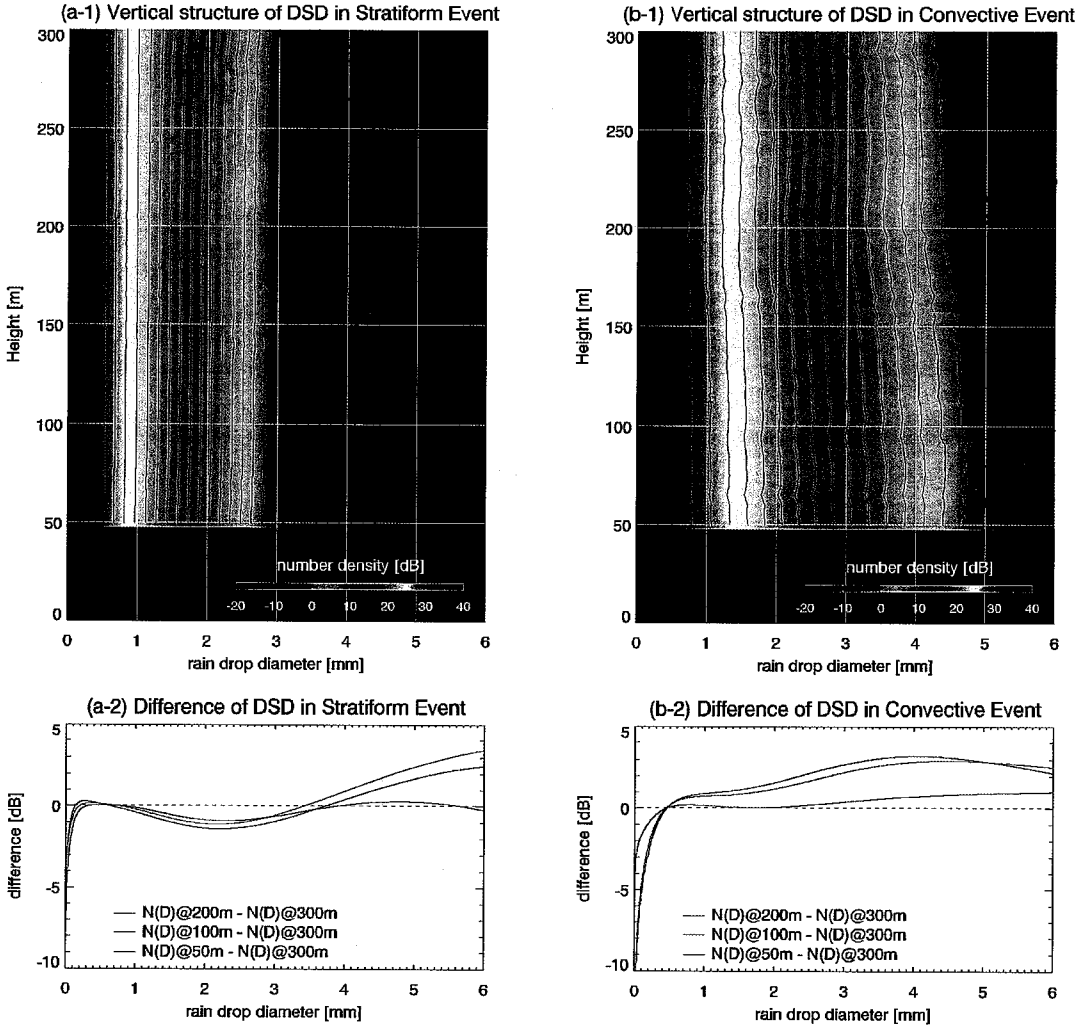

Figure 4.3: Vertical structures of DSD. (top left and top right) Results of stratiform and convective events, respectively. The colors represent number density (m^{-3} mm^{-1}) in dB. Contour lines are depicted with a 2 dB interval. (bottom) Differences of DSDs at different altitudes in each event. Black, blue, and red lines correspond to DSD differences of 200 m, 100 m, and 50 m, respectively, from 300 m in altitude.

Table 4.2: *Z-R* relations (the convective event)

BBR				
50 m	100 m	200 m	300 m	2DVD
$Z = 378R^{1.42}$	$Z = 378R^{1.43}$	$Z = 385R^{1.44}$	$Z = 405R^{1.43}$	$Z = 319R^{1.42}$

Chapter 5

A small-baseline weather radar network consisting of the Ku-band broadband radar

5.1 Introduction

A small-baseline weather radar network consisting of the BBR (the BBR network) covers a wide area without unobservable areas near ground by the collaborative operation. Precipitation are observed multi-directionally by several BBRs, and the products have high estimate accuracy. In this chapter, the BBR network deployed in Osaka is described. Also, a solution using multi-radar observation for precipitation attenuation by a radar, which is an inherent and significant problem for precipitation observation, is presented. Section 5.2 describes the deployment of BBRs in Osaka, and initial observations of the radar network with two BBRs. High-quality images by integrating both the BBRs in the indicated manner are also shown. Section 5.3 presents a correction method for precipitation attenuation proposed for the BBR network. This method does not only correct precipitation attenuation but also retrieve DSD in each range bin. The estimate accuracy is assessed by the simulation. Section 5.4 summarizes this chapter.

5.2 The Ku-band broadband radar network

5.2.1 Deployment of the Ku-band broadband radar network in Osaka

Two BBRs have already been deployed in Osaka. The characteristics of location of the BBRs are shown in Table 5.1. As shown in Figure 5.1, one is installed on top of a building in Toyonaka campus, Osaka University, Osaka, Japan (This radar is called "Toyonaka radar", hereafter). Another (shown in Figure 5.2) is installed on a building in Osaka works of Sumitomo Electric Industries, Ltd., Osaka, Japan (This is called "SEI

Figure 5.1: Overview of Toyonaka radar.

radar", hereafter). The baseline interval of both radars is about 14.32 km, and the area covered by both BBRs is about 294.18 km^2 in a surface of the ground, which is calculated in a maximum range of the BBR of 15 km. When observing up to 20 km with a modified observation mode (Instead of the maximum range, sensitivity gets worse.), the overlapped area increases to 696.32 km^2.

Now SEI radar has many obstacles closely around, and the view of SEI radar is limited as shown in the initial observation results. Therefore, in the near future, SEI radar will be moved to a site having less obstacles. One more BBR will be deployed in Nagisa sewage plant. We consider the three BBR network, which will cover north Osaka area as Figure 5.3, is a test bed of the BBR network for both the evaluation and operation.

5.2.2 Initial observation results

Observational characteristics are shown in Table 5.2. The interference between two BBRs are avoided by transmitting waves of different frequency bands (15.73 through 15.75 GHz and 15.75 through 15.77 GHz). In this observation, both Toyonaka and SEI radar observe whole sky (120 directions for azimuth, and 30 directions for elevation with

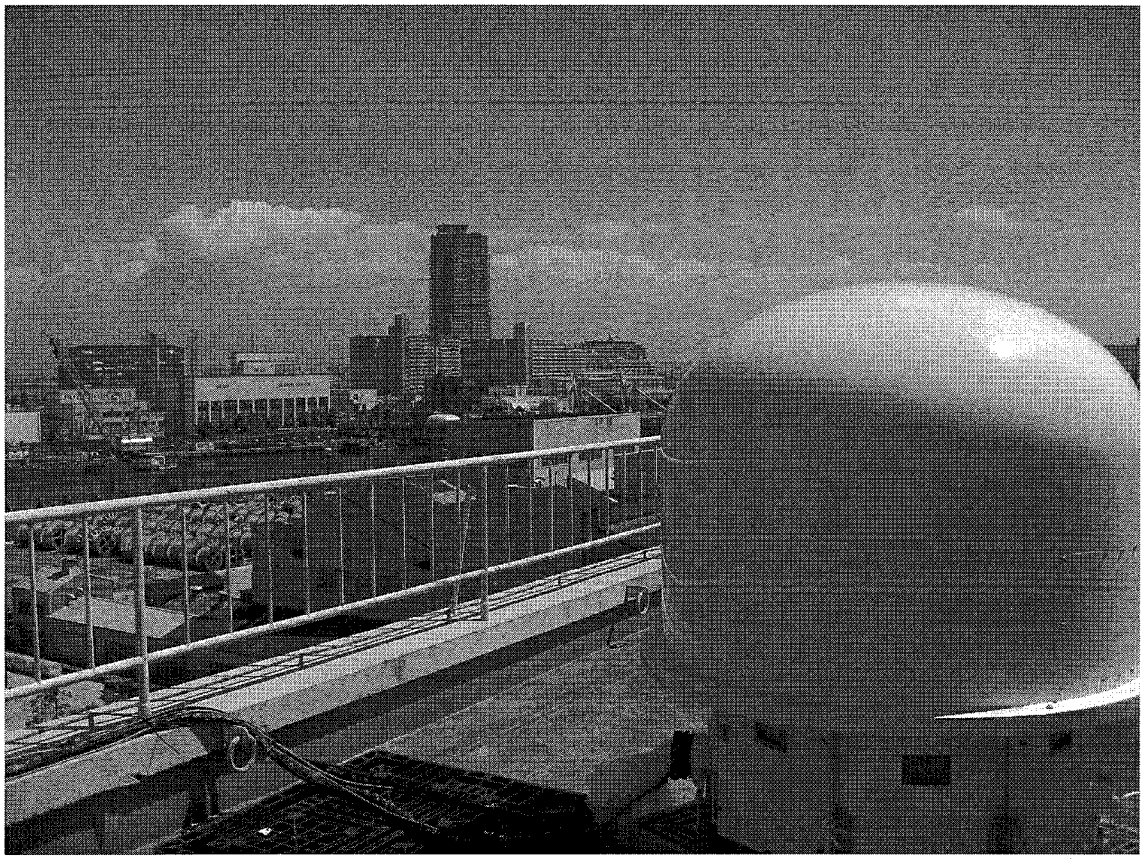

Figure 5.2: Overview of SEI radar.

Table 5.1: Characteristics of each radar site

Items	Toyonaka radar	SEI radar	Nagisa radar
Latitude	34.804939°N	34.676993°N	34.840145°N
Longitude	135.455748°E	135.435054°E	135.659029°E
View	Fine	Poor (Many obstacles notably for south and north-east)	Fine
Remarks		Temporally installed	From Apr., 2011

a 3-dB beam width of 3 deg) with an update rate of 64 s not in time synchronization. The time synchronization between BBRs will be achieved with use of global positioning system (GPS) in the near future. Therefore, we show results in a case of weather phenomena without any extreme change within 1 minute in this section. Initial observation results of reflectivity factor in an altitude of 1000 m in any one minute for five minutes

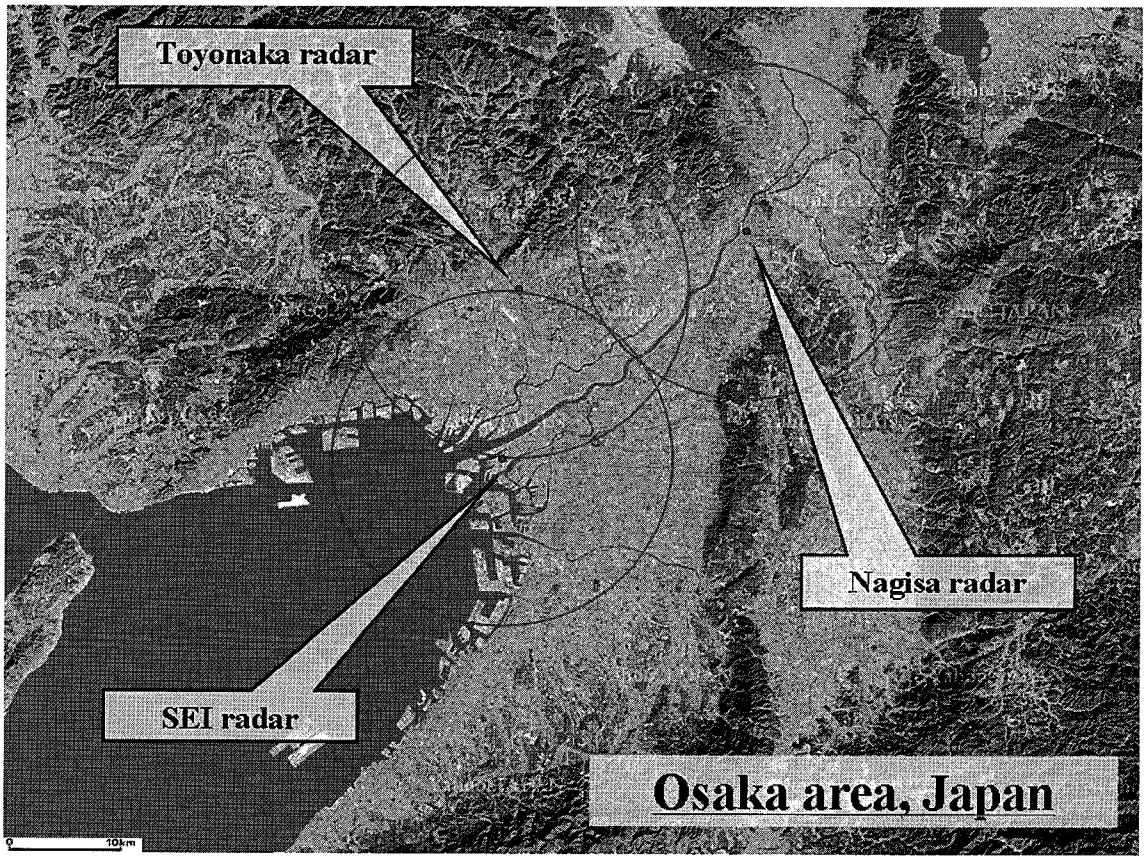

Figure 5.3: Deployment of the BBR network.

(from 13:54 to 13:59 on Sep. 14, 2010) are shown in Figure 5.4. Toyonaka radar (Panels (a-1) through (a-5)) cannot detect some north-east directions due to a lightning rod. Since SEI radar (Panels (b-1) through (b-5)) is interfered by many obstacles around, the received data indicate that the inputs of ADC are saturated in most directions for south and two directions for north-east. Additionally, SEI radar received more coupling noises due to the same cause. Precipitation attenuation is not corrected since it is considered that the affection is small in this case. In spite of these blockage, the two BBRs detected the same pattern of precipitation in the overlapped area with the high resolution, and the data integration of the BBR network provided impressive results. Panels (c-1) through (c-5) show the integrated reflectivity Z_{eINT} of both radars plotted on every 20 m planar grid in the overlapped area. In these panels, the precipitation pattens (especially, the pattern of zonal ranges around 5 km and meridional ranges from -10 to -2 km) were realistically clarified. The blind area of the SEI radar by the saturation (a zonal range of 9 km and a meridional range of -6 km, roughly) were retrieved by the Toyonaka radar (due to a simple method described below). Noisy areas of the SEI radar were also restored by the Toyonaka radar with high SNR. Thus, in the BBR network, one BBR supports in an area not observed well by another BBR. Furthermore, the data integration is easily and accurately

Table 5.2: Observation characteristics

	Toyonaka radar	SEI radar
Day and time	13:00 - 18:00, Sep. 14, 2010	13:00 - 18:00, Sep. 14, 2010
Operation mode	Spiral	Spiral
Azimuth rotation speed	30.0 RPM	30.0 RPM
Elevation	0 - 90°	0 - 90°
Power	10 W (peak)	10 W (peak)
Pulse length	160 μs	160 μs
Inter pulse period	260 μs	260 μs
Pulses / segment	64	64
Waveform	Linear up-chirp	Linear up-chirp
Frequency	15.73 - 15.75 GHz	15.75 - 15.77 GHz
Weighting window	Raised-cosine window (α=0.1)	Raised-cosine window (α=0.1)

performed in the BBR network since the observation delay between the BBRs are within 1 min. For example, in the case of 4 min delay, we must integrate Panels (a-1) and (b-5) in which their shapes, positions, and magnitudes of precipitation do not clearly agree. When they are merged without any assumption and with a simple method mentioned above, the shapes are stretched wider and heavy-rain cells are blinded. Therefore, the BBR network provides high-quality images by complimenting each other BBR, and these initial results suggest the availabilities to detect and analyze small-scale phenomena.

Integration of the BBRs' Data

- Step 1: Conversion to a Cartesian coordinate

  The data obtained by a weather radar are on a polar coordinate whose origin is the radar. In order to integrate data of BBRs positioned at different sites, all the data obtained by BBRs is converted from a polar coordinate to a Cartesian coordinate with use of Cressman weight function [35], which is one of the most popular methods in radar meteorology. Reflectivity factor at a desired point (r, θ, ϕ) is calculated by four points on four adjacent beams in the same range as shown in Figure 5.5. When reflectivity factors of the four adjacent points are Z_{en} where $n = 1$ through 4 and their coordinates are (r, θ_n, ϕ_n), a reflectivity factor at the desired point Z_e is expressed as

$$Z_e = \frac{\sum_{n=1}^{4} w_{cn} Z_{en}}{\sum_{n=1}^{4} w_{cn}}, \tag{5.1}$$

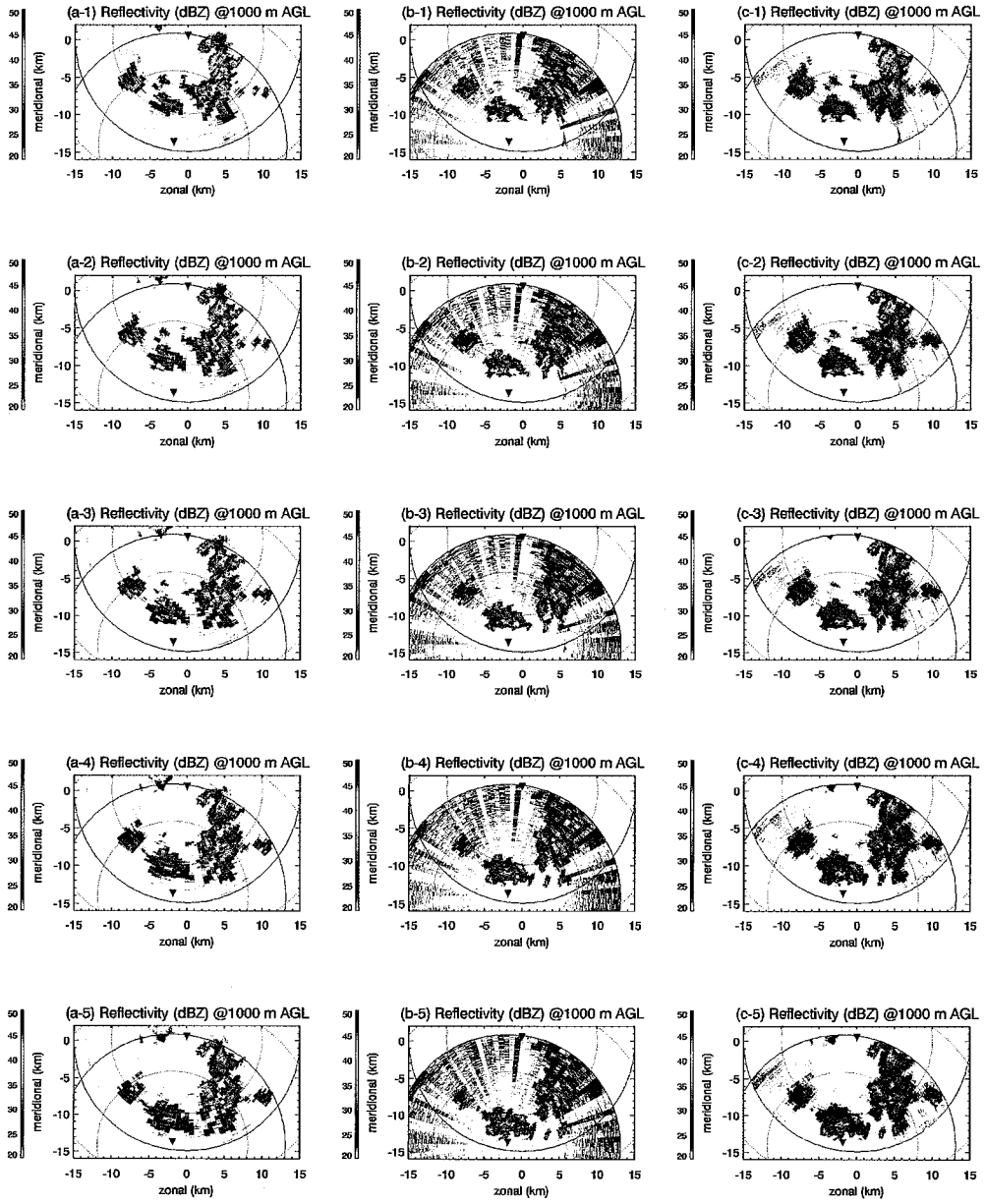

Figure 5.4: Initial Observation results at 13:54, 55, 56, 57, and 58. Top (Panels (a-1) through (a-5)) and middle (Panels (b-1) through (b-5)) panels are results of Toyonaka and SEI radar, respectively. Bottom panels (Panels (c-1) through (c-5)) are integrated results from both radars. In each panel, upper and lower triangles indicate Toyonaka and SEI radar, respectively. Black lines are on a range of 15 km from radars. Dot lines are on ranges of 10, 20, and 30 km.

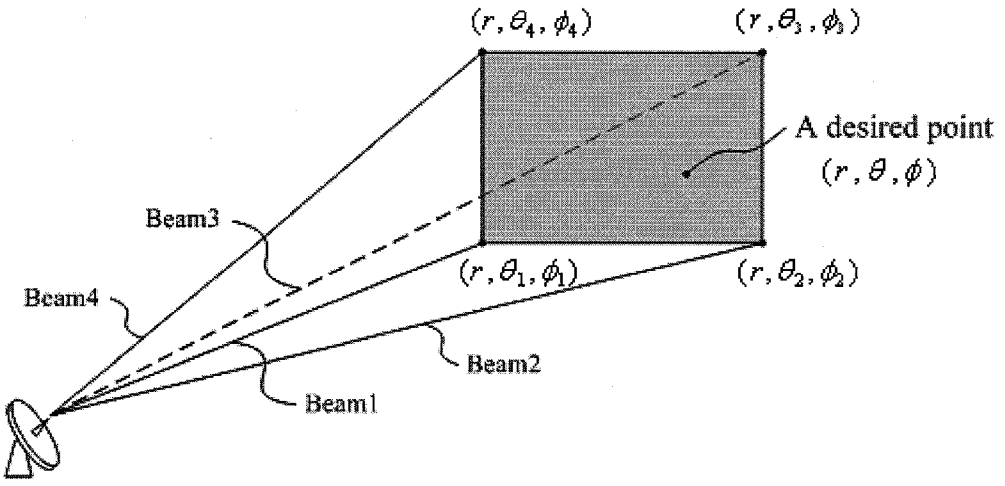

Figure 5.5: Description of the conversion from a polar to a Cartesian corrdinate.

where

$$w_{cn} = \frac{\theta_h^2 - ((\phi_n - \phi)^2 + (\theta_n - \theta)^2)}{\theta_h^2 + ((\phi_n - \phi)^2 + (\theta_n - \theta)^2)}. \tag{5.2}$$

θ_h is 3-dB beam beam width. Equation 5.2 is known as Cressman function. Conventionally, not only four adjacent points, more points positioned near a desired point is used. In this chapter, however, only four points are used for computational efficiency.

In the BBR network, each radar has reflectivities at four points on four adjacent beams to calculate that at a desired grid point. When reflectivities at a few points of them are significantly high values due to ground clutter or saturations, they can be rejected as outliers.

– Step 2: Integration of data obtained by BBRs

Data obtained by the two BBRs and converted to a Cartesian coordinate are averaged in this step. Integrated reflectivity Z_{eINT} is

$$Z_{eINT} = \frac{w_{r1} Z_{eBBR_1} + w_{r2} Z_{eBBR_2}}{w_{r1} + w_{r2}}, \tag{5.3}$$

where

$$w_{rn} = \frac{1}{r_n^2}. \tag{5.4}$$

r_n is range from n-th BBR. r_n^2 is proportional to a resolution volume, that is, this weighted averaging is based on the assumption that higher accuracy is achieved by higher resolution.

5.3 Correction algorithm for precipitation attenuation

5.3.1 Background

The radar equation with attenuation is expressed as

$$P_r(r) = \frac{C|K|^2 Z_m(r)}{r^2}, \tag{5.5}$$

where $P_r(r)$ is received power (W) at a range of r (m), C is radar constant, and $K = (n^2-1)/(n^2+2)$. n is complex index of refraction for liquid water. Measured reflectivity factor Z_m is related to equivalent reflectivity factor Z_e as

$$Z_m(r) = Z_e(r) / \exp\left[0.2 \ln 10 \int_0^r k(s) ds\right]. \tag{5.6}$$

It is empirically known that attenuation coefficient k (dB km^{-1}) is denoted by an exponential function of Z_e as Figure 2.1. Using a k-Z_e relation as

$$k(r) = \alpha Z_e(r)^\beta, \tag{5.7}$$

the analytical solution for precipitation attenuation, called Hitschfeld-Bordan (HB) solution, has been proposed [40]. HB solution is expressed as

$$Z_e(r) = Z_m(r) \exp[1 - 0.2\beta \ln 10 S(r)]^{-1/\beta}, \tag{5.8}$$

where

$$S(r) = \int_0^r \alpha Z_m(s)^\beta ds. \tag{5.9}$$

However, it is known that HB solution is unstable and often outputs unacceptably large errors, especially in a heavy rain event. In order to suppress these errors, several modified method for HB solution, the iteration method [41] and surface-referenced methods [42], [43], have been proposed for airborne or space-borne precipitation radars, and the estimate accuracies have been assessed [39]. These methods modify HB solution not to output large errors by an approximation or adjustment for a k-Z_e relation. The reflectivities retrieved by these methods are clearly improved, compared with HB solution, but an estimation error rapidly increases as advancing in range also in these modified methods. This is because they are deterministic approaches in which an error at a range bin is never suppressed and left to the adjacent bin. A k-Z_e relation significantly changes in different precipitation events (convective or stratiform), and, even in an event, it has several

variability. On the other hand, a stochastic approach has been proposed for a surface-referenced space-borne radar [44]. Since a Kalman filter is applied over range, instead of time, in this method, an error at a range bin is suppressed in stochastic sense. It has been shown that this stochastic approach is superior to deterministic approaches, however, an applied k-Z_e relation, which is defined as unique in a beam in this method, generates large errors.

Variability of a k-Ze relation depends on DSD which changes spatially and temporally. Chapter 4 indicated good agreement between DSDs estimated from the BBR and measured by 2DVD [15]. In this chapter, we propose a new method to correct for precipitation attenuation for the BBR network. This method is roughly separated in the Single-path retrieval (SPR) and the Networked retrieval (NTR). The SPR is a method to retrieve reflectivity along a beam path from a BBR by using one BBR. Assuming a relation between precipitation profiles in adjacent range bins and adopting DSD estimated from VDS at the lowest range bin as an initial condition, a Kalman filter approach is applied. This method also assumes the Gamma DSD, and the parameters of the Gamma DSD are defined as state variables of a Kalman filter. Therefore, the assumption of a unique k-Z_e relation is eliminated. This stochastic approach gives us uncertainties of state variables, which play an important role to integrate products of another BBR in the BBR networks. In the NTR, an optimal estimation using retrievals from several BBRs is achieved with use of the uncertainties. In addition, it is known that uncertainties are important for data assimilation to numerical weather models [45].

5.3.2 The single-path retrieval

In this section, the SPR which is used in an operation of one BBR. The SPR corrects precipitation attenuation in a beam path, as described in Panel (a) of Figure 5.6. In this method, the Gamma DSD and a N_0-μ relation respectively expressed as Equation 4.3 and 4.4 are assumed. Note that, the restriction of D in Equation 4.3 is not applied here. On these assumptions, the two parameter, μ and Λ, determine DSD. A Kalman filter is roughly separated as a prediction and a filtering process. The prediction is expressed as below.

$$\begin{aligned} \mu_{n+1} &= \mu_n + w_\mu, \\ \Lambda'_{n+1} &= \Lambda'_n + w_{\Lambda'}, \\ PIA_{n+1} &= PIA_n + \Delta r k(\mu_n, \Lambda'_n), \end{aligned} \tag{5.10}$$

where state variables of the Kalman filter are two DSD parameters, μ and Λ', and path-integrated attenuation PIA ($PIA(r) = \int_0^r k(s)ds$). Since it is known that Λ is from 0.48 to 17.34 (mm^{-1}), a transformation as below defines a new parameter Λ'.

$$\Lambda := \frac{16.86}{1+\exp(-\Lambda')} + 0.48. \tag{5.11}$$

A subscript of n indicates the n-th range bin in a beam path from the BBR. k corresponds Equation 4.6. System noises of two DSD parameters are w_μ and $w_{\Lambda'}$. A standard deviation

of w_μ and $w_{\Lambda'}$, σ_μ and $\sigma_{\Lambda'}$, are set to, respectively, 1×10^{-4} (m^{-1}) and 0.17 (mm^{-1} m^{-1}), assuming variabilities in a general precipitation event. In the prediction, a DSD in the n-th range predicts a DSD in the adjacent bin having the same mean as itself, and PIA_{n+1} is equal to a sum of PIA_n and the attenuation at the n-th bin. State variables express an observational value, Z_m, as

$$Z_{mn} = Z_e(\mu_n, \Lambda'_n) - 2PIA_n + v, \tag{5.12}$$

where v is an observational noise which is set to 1.4 (dBZ), considering fluctuations of radar signals returned from precipitation media [21]. As k is determined from DSD and σ_e as Equation 4.6, Z_e is also determined from DSD and back scattering cross section σ_b (mm^2) due to Mie theory [13] as

$$Z_e = \frac{\lambda^4}{\pi^5 |K|^2} \int_0^\infty \sigma_b(D) N(D) dD. \tag{5.13}$$

The observational value is used for the filtering process. Since both equations of the prediction and the filtering include non-linear functions, it is necessary to apply an extended Kalman filter, which is an approximation of a Kalman filter to apply for a non-linear dynamic system [46]. Initial conditions of the DSD parameters are obtained in the same way presented as Section 4.3. An initial DSD estimated from a VDS of the nearest range bin is applied to initial DSDs in all the beam path. Also, $PIA_0 = 0$ (transmitted power is never attenuated by precipitation in the nearest range) is applied. It is likely to assume these initial conditions by the nearest range of 50 m, that is, no attenuation and uniformity of precipitation in the small region within 50 m are assumed easily.

A Kalman filter assumes that all the variables is a Gaussian stochastic variable. This is why estimate values in each range bin are determined by two parameters, mean values and a covariance matrix. The operation with one BBR needs only mean values in each range bin. Covariances play an important role to integrate data of several BBRs in the NTR shown as the next section.

5.3.3 The networked retrieval

In the BBR network, retrievals with high accuracy are achieved due to measurements multi-directionally observed by several BBRs. Panel (b) of Figure 5.6 describes a network with two BBRs. The two BBRs has many cross points of beams, as indicated by black dots. Due to the high temporal resolution of the BBR, it is likely that the same precipitation profiles at cross points in one VoS (within about 1 minute).

The NTR consists of four steps.

- Step 1: The SPR

  The SPR is performed in each beam on both BBRs. Here, not only mean values but also covariances of each estimate in each range bin are saved.

– Step 2: Trade of data at cross points

All the estimate values (mean and covariance) at cross points are traded between the two BBRs. A mean value of PIA is calculated in a manner below.

$$\begin{aligned} \mu_a &= \mu_b, \\ \Lambda'_a &= \Lambda'_b, \\ PIA_a &= Z_e(\mu_b, \Lambda'_b) - Z_m, \end{aligned} \tag{5.14}$$

where subscripts, a and b, means data after and before trading at a cross points, respectively. Here, Z_m is an observation value of a BBR of the received side of data at the cross point. A covariance is traded without any conversion.

– Step 3: Retrievals starting with traded cross points

When estimates of one point are traded, two retrievals advancing toward and against the BBR starting with a cross point are performed in the beam path. Against the BBR, retrievals are performed in the same way of the SPR starting with the traded data. On the other hand, In retrievals toward the BBR, the prediction is expressed as

$$\begin{aligned} \mu_{n-1} &= \mu_n + w_\mu, \\ \Lambda'_{n-1} &= \Lambda'_n + w_{\Lambda'}, \\ PIA_{n-1} &= PIA_n - \Delta rk(\mu_n, \Lambda'_n). \end{aligned} \tag{5.15}$$

The retrieval of this step is performed as many times as the number of traded cross points. The estimate values of all the range bins are saved.

– Step 4: Optimal estimation

All the retrievals are optimally averaged in each range bin by using covariances as below.

$$\begin{aligned} \mathbf{x} = (\Sigma_{SPR}^{-1} + \Sigma_{TRD_1}^{-1} + \Sigma_{TRD_2}^{-1} + \cdots + \Sigma_{TRD_K}^{-1})^{-1} \\ (\mathbf{x}_{SPR}\Sigma_{SPR}^{-1} + \mathbf{x}_{TRD_1}\Sigma_{TRD_1}^{-1} + \mathbf{x}_{TRD_2}\Sigma_{TRD_2}^{-1} + \mathbf{x}_{TRD_K}\Sigma_{TRD_K}^{-1}), \end{aligned} \tag{5.16}$$

where

$$\mathbf{x} = [\ \mu \ \ \Lambda' \ \ PIA\ ]^T, \tag{5.17}$$

$$\Sigma = E[\mathbf{x}\mathbf{x}^T]. \tag{5.18}$$

Subscripts of SPR and TRD indicates retrievals of Step1 and Step3, respectively. K is the number of the traded cross points. $E[\cdot]$ means the expectation.

A Kalman filter is equivalent to a maximum likelihood estimation in a linear dynamic system. If equations of the prediction or the filtering are expressed by linear functions, networked retrieval could be presented in a more simple form which is a Kalman smoother with use of the traded data. However, it is difficult for a Kalman smoother to be applied in a non-linear system. In this method, an approximation of a Kalman smoother is obtained by assuming that each retrievals are dependent each other and averaging them with the covariances in each range bin.

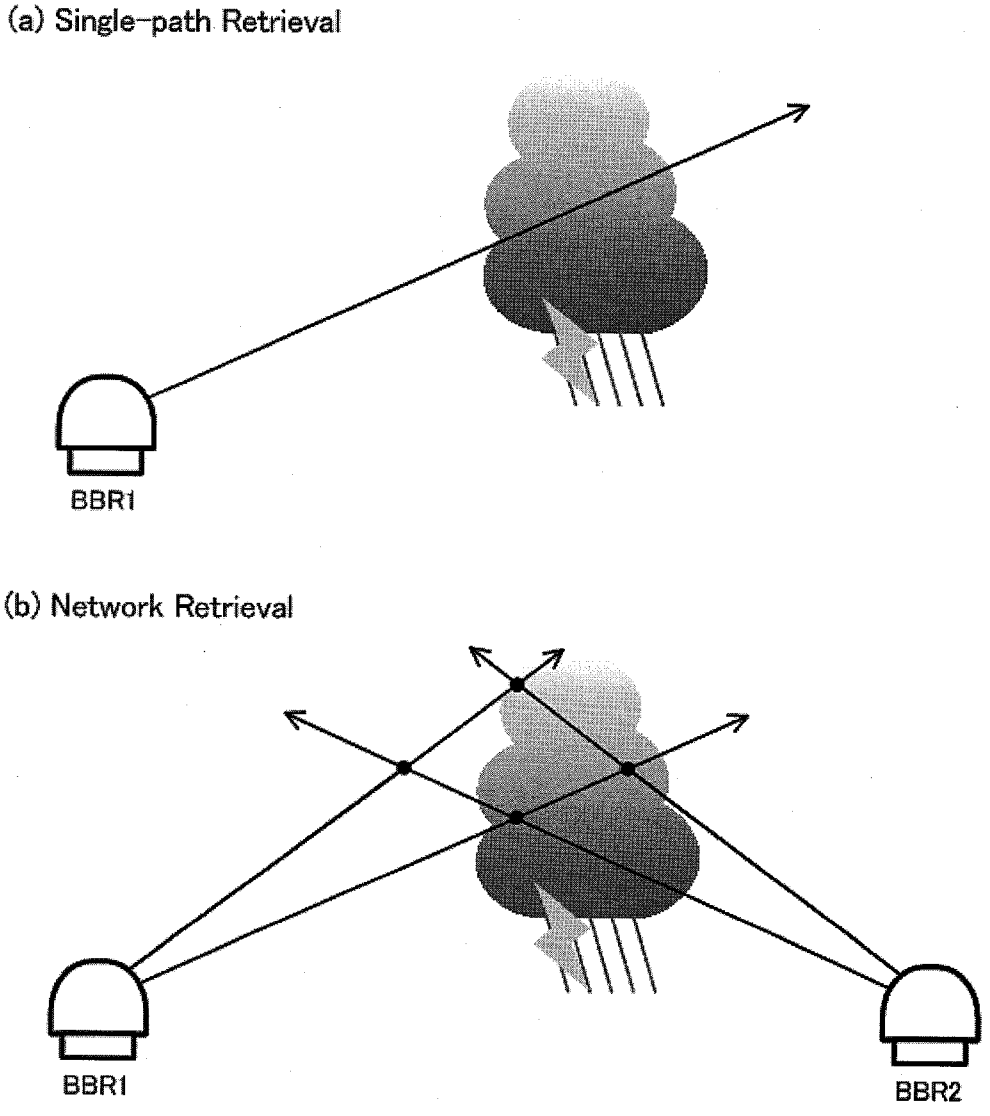

Figure 5.6: Descriptions of the proposed method. Panel (a) and (b) describe the SPR and the NTR, respectively. For simplicity, a network with two BBRs are described in Panel (b). Arrows indicate beams. Dots indicate cross points of beams of two BBRs.

5.3.4 Simulation

In order to validate performances of the proposed method, radar signal simulations are carried out.

Simulation model

In simulation models, parameters of the Gamma DSD, μ and Λ, are defined in all the range bins in all the directions. N_0 is determined from μ with use of Equation 4.4. Z_e and k are respectively determined from DSD as Equation 5.13 and 4.6, and then, determines Z_m as Equation 5.6. Also, Z_m includes fluctuations corresponding SNR, IPP, and spectral width as statistical property of Z_m shown in [21]. In this chapter, a model simulates a single cell of precipitation (simulated by Gaussian spatial shape of μ and Λ) including heavy precipitation of about 50 dBZ (roughly corresponds to a rainfall rate of 100 mm h^{-1} as shown in Figure 5.7. Panels (a), (b), and (c) shows a planar distributions of μ, Λ, and Z_e with the horizontal and vertical axes corresponding to zonal and meridional (km). The two BBRs, BBR1 and BBR2, are positioned at coordinates of (-7,0) and (7,0), respectively. White lines indicate directions of beams. Black dash line is a sample focused on especially to validate the performances in the next subsection. The model is digitized by 3-dB beam width, and Z_e and Z_m for each BBR as shown in Figure 5.8 and 5.9, respectively.

Table 5.3: Characteristics of simulation

Frequency	15.75 GHz
Inter pulse period	238 μs
Noise level	12 dBZ at 15 km
Complex index of refraction	(7.3, -2.4)
Spectral width	1.5 m s^{-1}

Simulation results

The simulation results of estimations for Z_e, Λ, and μ on the focused line are, respectively, shown in Figure 5.10, 5.11, and 5.12 in which the horizontal axis is range (m). In Figure 5.10, the truth of Z_e and Z_m in this simulation are indicated by the black and green lines, respectively. HB solutions with k-Z_e relations of $k = 3.45 \times 10^{-4} Z_e^{0.834}$ (a statistical average from observations of 2DVD shown in Figure 2.1) and $k = 4.60 \times 10^{-4} Z_e^{0.714}$ (calculated by the initial condition of DSD in this simulation model in a manner shown in [37]) are indicated by the purple and light-blue lines, respectively. The purple line is a result of overestimation of HB solution. Over a range of 9.5 km, retrieved reflectivity reached an infinite value. This is because k calculated by the former k-Z_e relation is larger

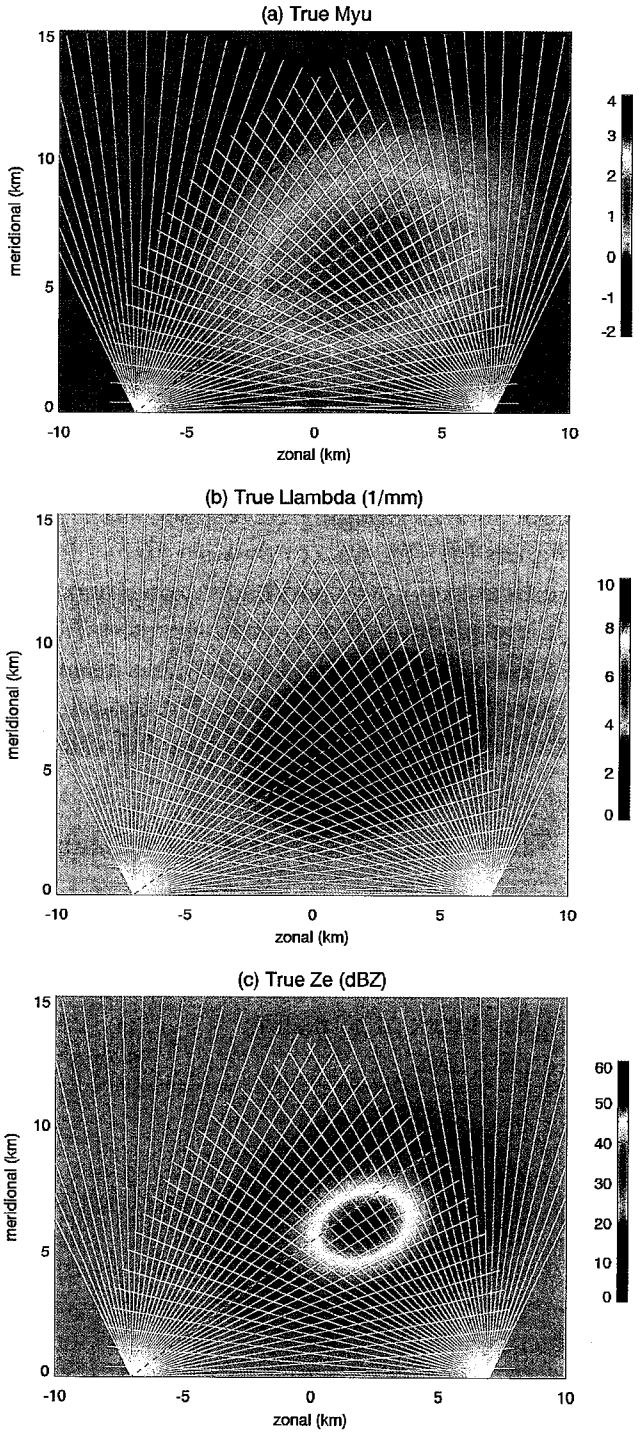

Figure 5.7: Simulation model. Panel (a), (b), and (c), respectively, shows the planer distribution of μ, Λ, and Z_e with the horizontal and vertical axes corresponding to zonal and meridional (km). BBR1 and BBR2 are deployed at coordinates of (-7,0) and (7,0), respectively. White lines indicate beam paths of both the BBR. Retrieval capabilities on black dash line are assessed in the next subsection.

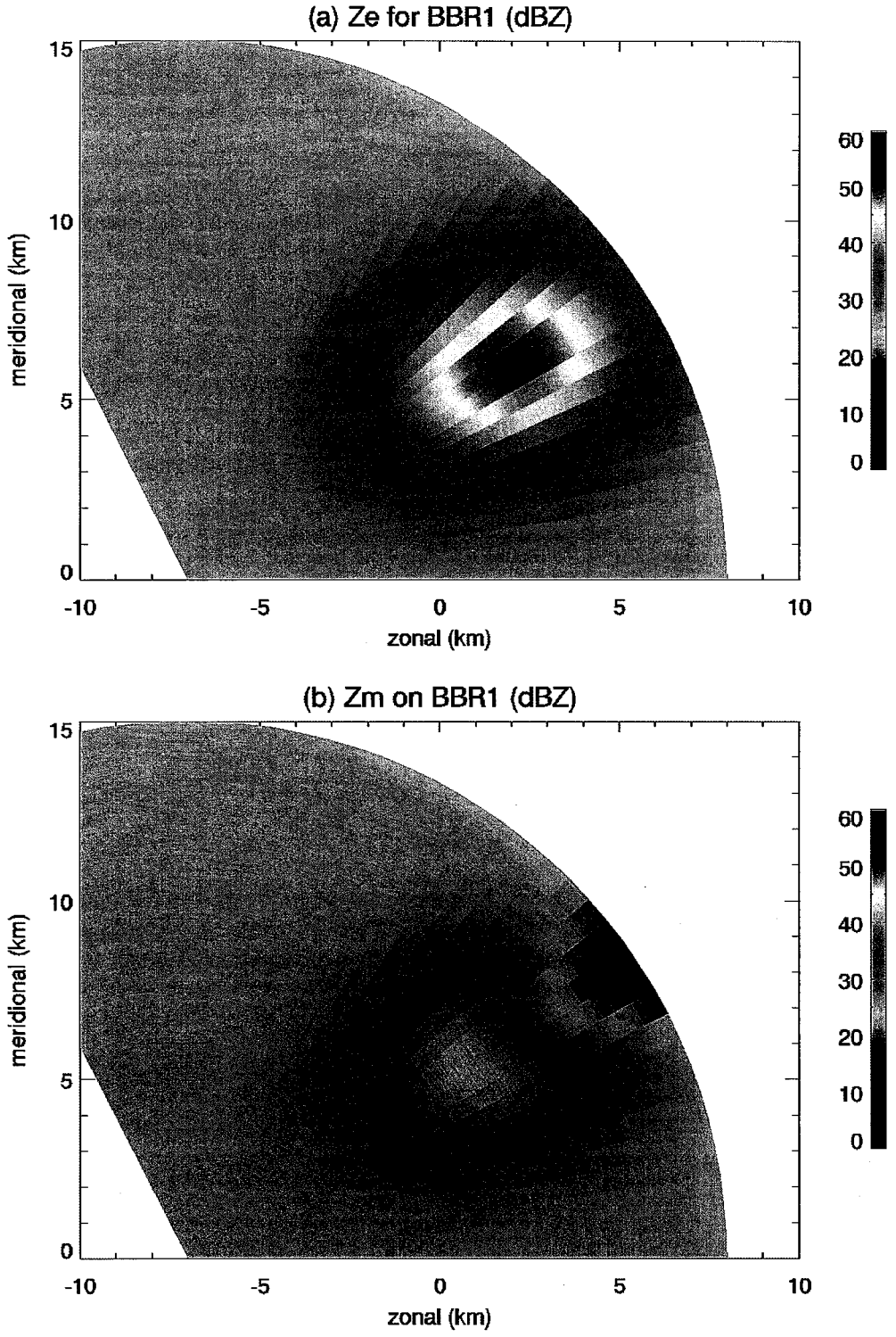

Figure 5.8: Z_e and Z_m seen from BBR1 with the horizontal and vertical axes corresponding to zonal and meridional (km). Both parameters are digitized by 3°-beam width.

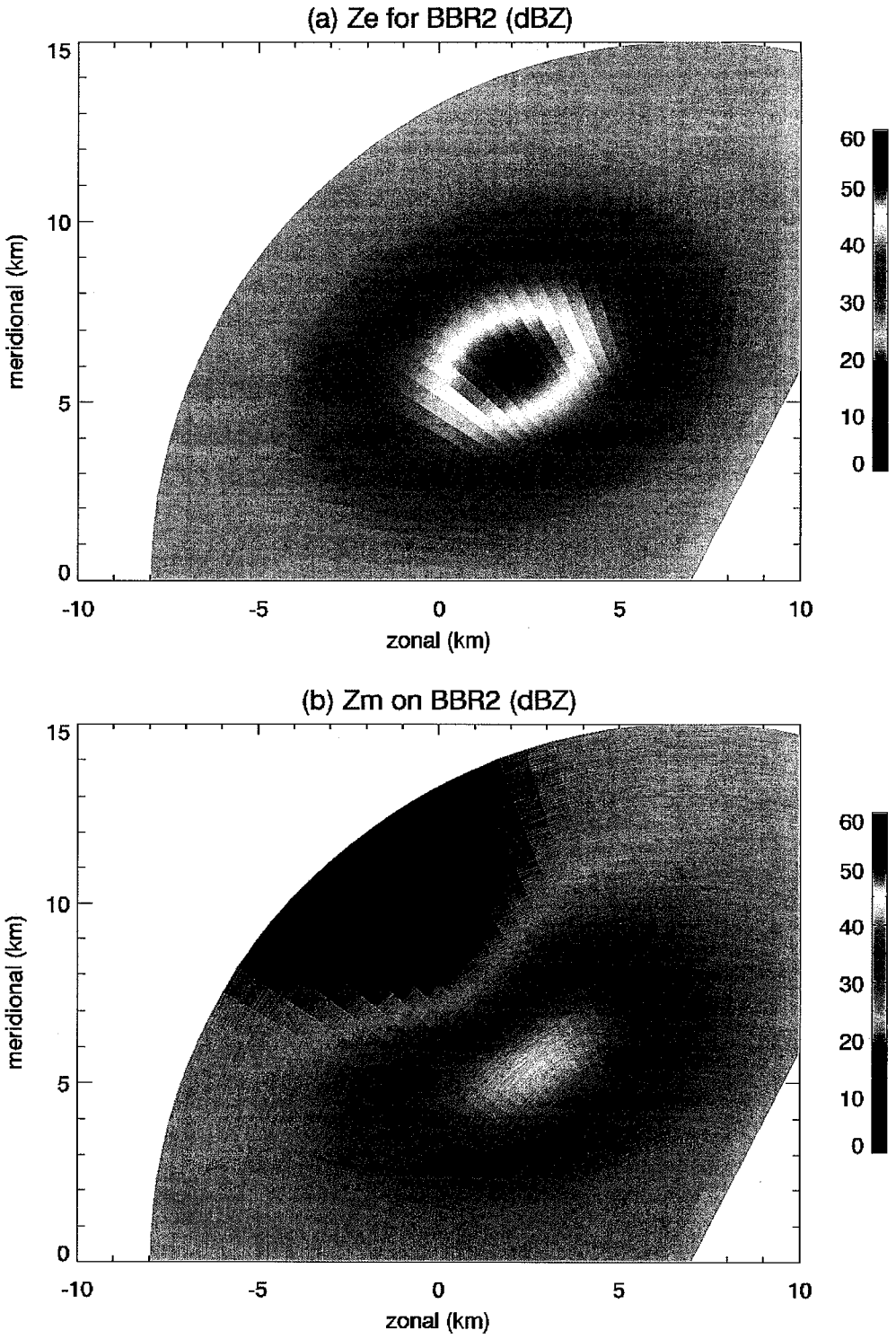

Figure 5.9: Z_e and Z_m seen from BBR2 with the horizontal and vertical axes corresponding to zonal and meridional (km). Both parameters are digitized by 3°-beam width.

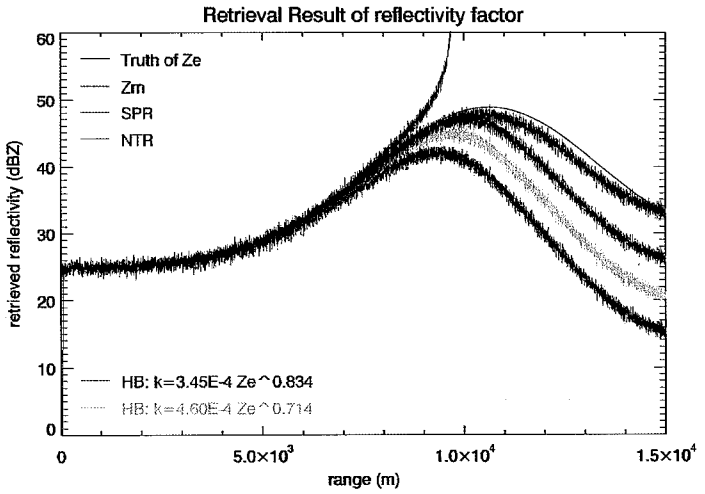

Figure 5.10: Retrieval result of Z_e (dBZ) on the focused beam path. Black and green line indicate the truth of Z_e and Z_m in this simulation, respectively. Purple and light-blue line present Z_e retrieved by HB solutions with the k-Z_e relations of $k = 3.45 \times 10^{-4} Z_e^{0.834}$ and $k = 4.60 \times 10^{-4} Z_e^{0.714}$. Blue and red line indicate retrieval results of the SPR and the NTR.

than that in the simulation. On the other hand, the light-blue line shows a result of underestimation because k of the latter k-Z_e relation at the site of BBR1 is smaller than that at other range bins. The error is about 15 dBZ at most at a range of 15 km. These two HB solutions showed that it is difficult to retrieve Z_e accurately in using a deterministic approach with a unique k-Z_e relation in a beam path. A result of the SPR is shown by the blue line which indicates underestimation due to use of the k-Z_e relation of the initial condition, however, the errors are about half of the latter HB solution (light-blue one). The NTR, indicated by the red line, achieved an accurate retrieval, whose error is a few dBZ even at most, better than any method shown in this figure. This is because estimations of BBR2 corrects the errors in the SPR of BBR1 optimally. In Figure 5.11, the truth of this simulation is indicated by the black line, and retrieval results of Λ of the SPR and the NTR are shown by the blue and red line, respectively. The maximum error of both method are 0.5 mm^{-1}, and it is shown that the NTR retrieves with more stability compared with the SPR. Both the retrievals are worse in the heavy-rain area. However, around 15 km range, retrievals of the NTR are more accurate than those of the SPR. In Figure 5.12, the truth of this simulation is indicated by the black line, and retrieval results of μ of the SPR and the NTR are shown also by the blue and red lines, respectively. μ is not retrieved well in these method because this parameter in much less dominant in the observation equation (Equation 5.12). While, in the SPR, μ has almost the same value in all the range bins, the NTR corrects them a little.

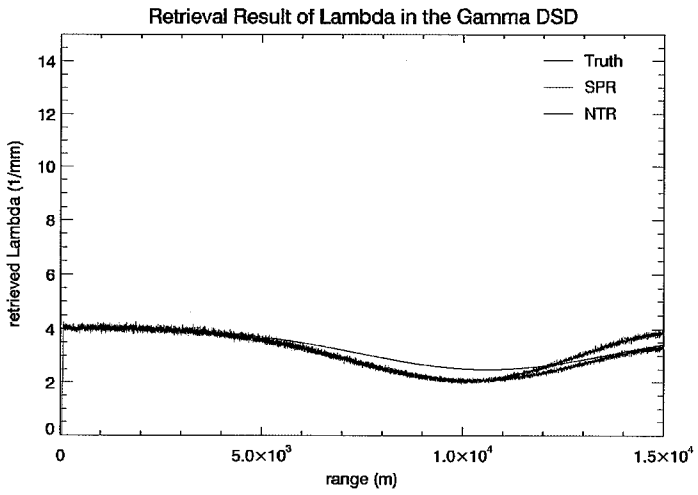

Figure 5.11: Retrieval result of Λ (mm^{-1}) on the focused beam path. Black line indicates the truth of Λ in this simulation. Blue and red line indicate retrieval results of the SPR and the NTR.

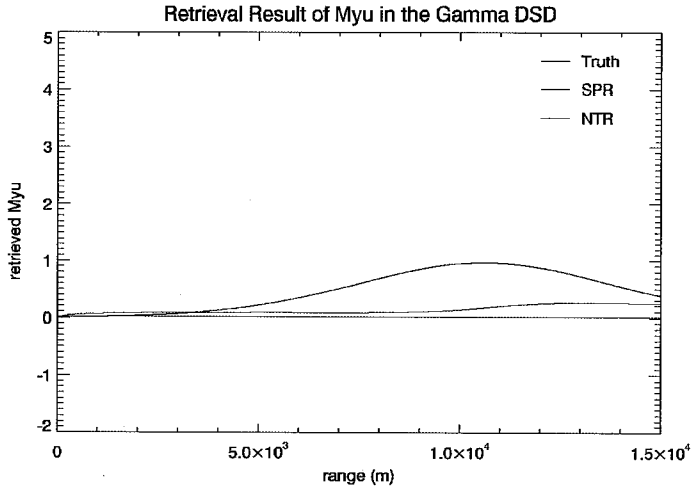

Figure 5.12: Retrieval result of μ on the focused beam path. Black line indicates the truth of μ in this simulation. Blue and red line indicate retrieval results of the SPR and the NTR.

5.4 Conclusion

We have proposed a new correction method for precipitation attenuation for the BBR network, which is a stochastic approach adopting a Kalman filter. Since the BBR accurately estimates DSD in closest several hundreds meters, a parameter of the Gamma DSD, μ and Λ, are adopted as a state variable. The SPR estimated precipitation properties with higher accuracy and stability than HB solution in the simulation. However, in an area with heavy precipitation, Z_e was underestimated. This is because the uncertainty of the state variables increases when *PIA* has a large mean value.

In an observation of two or more BBRs, the SPRs of BBRs are optimally integrated in a stochastic sense. In the simulation results, the NTR corrected the estimations of the SPR by using estimate values of another BBR. When an estimate value of another BBR at a cross point of beams has a lower uncertainty (*PIA* is low), a weighting average with a higher weight for the estimate value with the lower uncertainty in the optimal estimation. When an estimate of another has a higher uncertainty, it is averaged with a lower weight. In a radar network with more BBRs, the NTR should retrieve precipitation profiles with higher accuracy.

While Z_e and Λ were retrieved with high accuracy, μ was not estimated well. This is because μ is much less dominant on the observation equation (Equation 5.12) than the other two state variables of Λ and *PIA*. Another problem is that the number of the state variables ($= 3$) are more than that of the observed value ($= 1$) in this approach. In the future, we will develop the polarimetric BBR which gives us polarimeteric parameters of precipitation, differential reflectivity Z_{dr}, specific differential phase K_{dp}, and co-polar correlation coefficient between horizontal and vertical returns ρ_{co}. We will evaluate dependency of these polarimeteric parameters for μ and add in the observation equation in next upgraded algorithm.

In the NTR, the load for communication network is reduced by trading only data at cross points of beams between BBRs. However, the data trade must be performed as many times as square of the number of BBRs in this method, and the number of data trades will be an important problem in the network with the large number of BBRs. A strategy of data trading in large network of the BBRs with high efficiency also has to be validated. Furthermore, uncertainties obtained by this approach enable us to input all the estimate values into numerical weather models to predict weather phenomena. Accuracy of prediction for weather phenomena using the high-resolution data acquired by the BBR network will be validated in the future.

Chapter 6

Conclusion

In order to detect and predict small scale weather phenomena such as tornadoes and downbursts which seriously cause damage to our lives but are hardly detected by conventional weather radars, we have been proposing and developing the Ku-band broadband radar (BBR) network which is a small-baseline weather radar network with the BBR, a remarkably high-resolution Doppler radar.

In Chapter 2, a basic concept, configuration, signal processing, and general parameters of the BBR were presented. In the initial observation of the BBR held in Tanegashima island, Kagoshima, Japan, from 2008 to 2009, a tornado of F0 scale, a typhoon, and heavy rain events were observed. As an assessment of the observation accuracy for precipitation, a cross validation with a ground-based equipment of a disdrometer, which is co-located, showed an excellent agreement. Results of the spiral (volume-scanning) observation showed fine structures of small precipitation cells in any one minute. A comparison with a conventional C-band radar also indicated the validity of high-resolution observation by the BBR for small-scale hazardous phenomena.

In Chapter 3, an algorithm applied for the real-time operation in the BBR was presented. The BBR is more affected by ground clutter (reflections from ground, building, trees, and other static targets) than conventional radars since the observable range is very low and the BBR is occasionally installed in an urban or rugged mountainous area. In many methods proposed for ground clutter suppression, any method with high accuracy has also high computational costs. The algorithm proposed in this chapter suppresses ground clutter and estimates precipitation profiles, even when precipitation echo are overlapped with strong clutter in spectral domain. With assuming a Gaussian spectrum of precipitation and without high-cost calculations such as an inversion of a large matrix, a high accuracy and computational efficiency of this algorithm were achieved. The assessment results showed that the proposed algorithm has about two times higher computational costs and higher estimate accuracy for precipitation echo observed in the BBR than a conventional method of the moment method.

In Chapter 4, a scientific topic derived from observations on the BBR was presented. Vertical structure of raindrop size distribution (DSD) in atmospheric boundary layer is important to understand observational errors in radar observations. Especially, it is also

important for a study of global water cycle using a space-borne precipitation radar. However, it is difficult for all the conventional weather radars, including wind-profilers, and space-borne radars, to observe precipitation below an altitude of several hundred meters. The BBR observation provided the first report that the growth process increases about 2 times in the number of raindrops larger than 0.5 mm in diameter even below an altitude of 300 m in a convective event.

Chapter 5 described the deployment and characteristics of the BBR network installed in Osaka. At present, two BBRs are deployed and one more BBR will be equipped in next year, 2011. Initial results of simultaneous observations from the two BBRs were shown. The observation results of both BBRs are integrated in an indicated manner, and high-quality images of precipitation are output by complimenting each other. Also, a correction method for precipitation attenuation for the BBR network was presented. Precipitation attenuation is a critical and inherent problem for most precipitation radars since it often yields a large negative bias error which makes us underestimate reflectivity factor of precipitation. Therefore, it is essential for the BBR network to accurately correct precipitation attenuation since Ku-band waves are strongly attenuated more than those lower frequency bands. In a radar network with high temporal resolution, it is likely that precipitation does not change in a volume scan and physical parameters in a point seen from each radar are equivalent. A proposed method in this chapter corrects precipitation attenuation in a stochastic sense. A stable retrieval of the proposed method was output in a simulation of a heavy rain event, in which HB solutions output unacceptable large errors. This is because the stochastic properties allow us to optimally integrate precipitation profiles retrieved in each radar in this method.

In the future, we will develop the dual-polarimetric BBR. Dual-polarimetric measurements with high-resolution at Ku-band will give us more kinds of precipitation measurements, for example, oblateness of raindrops, their variability, and so on. The combined measurements of them should provide more insight regarding precipitation types and their evolution than the single-polarimetric measurements. In the network observation with the dual-polarimetric BBR, retrieval method for precipitation profiles presented in Chapter 5 could be extended to include the dual-polarimetric measurements and give us DSD information constantly in all observable area. Uncertainties of retrieved precipitation profiles enable us to input all the estimate values into numerical weather models to predict weather phenomena. It is expected by their fine measurements of precipitation to predict any weather phenomena accurately and compensate our safety.

List of Acronyms

ADC	:	Analog-to-Digital Converter
AGL	:	Above Ground Level
AWGN	:	Additive White Gaussian Noise
BBR	:	BroadBand Radar
CAPPI	:	Constant Altitude Plan Positioning Indicator
CASA	:	Collaborative Adaptive Sensing of the Atmosphere
CSR	:	Clutter-to-Signal Ratio
DAC	:	Digital-to-Analog Converter
DPR	:	Dual-frequency Precipitation Radar
DSD	:	rainDrop Size Distribution
DSP	:	Digital Signal Processor
FFT	:	Fast Fourier Transform
GMAP	:	Gaussian Model Adaptive Processing
GPM	:	Global Precipitation Measurement
GPS	:	Global Positioning System
HB	:	Hitschfeld-Bordan
HPA	:	High-Power Amplifier
IIR	:	Infinite Impulse Response
IPP	:	Inter Pulse Period
JWD	:	Joss-Waldvogel Disdrometer
LNA	:	Low-Noise Amplifier
LO	:	Local Oscillator
NTR	:	NeTworked Retrieval
PIA	:	Path-Integrated Attenuation
PR	:	Precipitation Radar
PTM	:	Parametric Time Domain Model
RHI	:	Range Height Indicator
SNR	:	Signal-to-Noise Ratio
SPR	:	Single-Path Retrieval
TRMM	:	Tropical Rainfall Measuring Mission
VDS	:	Vertical Doppler Spectrum
VoS	:	Volume Scan
X-net	:	X-band radar network
2DVD	:	2 Dimensional Video Disdrometer

Bibliography

[1] M. Skolnik (2008), Radar Handbook, Third edition, chap. 1, 1.1–1.24, *McGraw-Hill, New York, U.S.*

[2] R. A. House, Jr. (1993), Cloud Dynamics, chap. 4, 107–129, *Academic Press, California, U.S.*

[3] Y-L. Lin (2007), Mesoscale Dynamics, chap. 1, 1–11, *Cambridge Univ. Press, Cambridge, U.K.*

[4] H. Niino, T. Fujitani, and N. Watanabe (1997), A statistical study of tornadoes and waterspouts in Japan from 1961 to 1993, *J. Clim.*, vol. 10, no. 7, 1730–1752.

[5] J. T. Schafer and D. L. Kelly (1986), A minimum assumption tornado-hazard probability model, *J. Clim. Appl. Meteorol.*, vol. 25, 1934–1945.

[6] C. R. Williams, A. B. White, K. S. Gage, and F. M. Ralph (2007), Vertical structure of precipitation and related microphysics observed by NOAA profilers and TRMM during NAME 2004, *J. Clim.*, vol. 20, 1963–1712.

[7] E. I. Nikolopoulos, A. Kruger, W. F. Krajewski, C. R. Williams, and K. S. Gage (2008), Comparative rainfall data analysis from two vertically pointing radars, an optical disdrometer and a rain gauge, *Nonlinear processes Geophys.*, vol. 15, 987–997.

[8] K. S. Gage, C. R. Williams, W. L. Clark, P. E. Johnston, and D. A. Carter (2002), Profiler contribution to Tropical Rainfall Measurement Mission (TRMM) ground validation field campaigns, *J. Atmos. Oceanic Technol.*, vol. 19, 843–863.

[9] F. Junyent, and V. Chandrasekar (2009), Theory and characterization of weather radar networks, *J. Atmos. Ocean. Technol.*, vol. 26, 474–491.

[10] M. Maki et al (2008), X-band polarimetric radar network in the Tokyo metropolitan area - X-NET, paper presented at ERAD 2008, Finnish Meteorol. Inst., Helsinki.

[11] R. J. Doviak, and D. S. Zrnic (1993), Doppler Radar and Weather Observations, Second edition, chap. 2, 10–29, *Dover Publications, Inc., New York, U.S.*

[12] V. Chandrasekar, and S. Lim (2008), Retrieval of reflectivity in a networked radar environment, *J. Atmos. Ocean. Technol.*, vol. 25, no. 10, 1755–1767.

[13] F. T. Ulaby, R. K. Moore, and A. K. Fung (2007), Microwave Remote Seinsing: Active and Passive. Vol. 1, Microwave Remote Sensing Fundamentals and Radiometry, Second edition, chap. 5, 256–343, *Artech House, Norwood, MA, U.S.*.

[14] P. S. Ray (1972), Broadband complex refractive indices of ice and water, *Appl. Opt.*, vol. 11, no. 8, 1836–1844.

[15] A. Kruger and W. F. Krajewski (2002), Two-dimensional video disdrometer: A description, *J. Atmos. Oceanic Technol.*, vol. 19, 602–617.

[16] D. S. Zrnic, J. F. Kimpel, D. E. Forsyth, A. Shapiro, G. Crain, R. Ferek, J. Heimmer, W. Benner, T. J. McNellis, and R. J. Vogt (2007), Agile-beam phase array radar for weather observations, *Bull. Amer. Meteorol. Soc.*, vol. 88, no. 11, 1753–1766.

[17] J. D. Kraus and R. J. Marhefka (2002), Antennas for All Apprications, chap. 17, 607–635, *McGraw-Hill, New York, U.S.*.

[18] E. Yoshikawa, T. Mega, T. Morimoto, T. Ushio, and Z. Kawasaki (2009), Real-time spectral moments estimation and ground clutter suppression for precipitation radar with high-resolution, *IEICE Trans. Commun.*, vol. E92-B, no. 2, 578–584.

[19] R. J. Doviak, and D. S. Zrnic (1993), Doppler Radar and Weather Observations, Second edition, chap. 5, 87–121, *Dover Publications, Inc., New York, U.S.*.

[20] D. C. Dowell, C. R. Alexander, J. M. Wurman, and L. J. Wicker (2005), Centrifuging of hydrometers and debris in tornadoes: Radar-reflectivity patterns and wind-measurement errors, *Mon. Weather Rev.*, vol. 133, no. 6, 1501–1524.

[21] V. N. Bringi, and V. Chandrasekar (2001), Polarimetric Doppler Weather Radar: Principles and Applications, chap. 5, 211–293, *Cambridge Univ. Press, Cambridge, U.K.*.

[22] T. Ushio, S. J. Heckman, H. Christian, and Z. Kawasaki (2003), Vertical development of lightning activity observed by the LDAR system: Lightning bubbles, *J. Appl. Meteorol.*, vol. 424, no. 2, 165–174.

[23] T. Ushio, Z. Kawasaki, Y. Ohta, and K. Matsuura (1997), Broad band interferometric measurement of rocket triggered lightning in Japan, *Geophys. Res. Lett.*, vol. 24, no. 22, 2769–2772.

[24] S. Lim, V. Chandrasekar, and V. N. Bringi (2005), Hydrometer classification system using dual-polarization radar measurements: Model improvements and *in situ* verification, *IEEE Trans. Geosci. Remote Sens.*, vol. 43, no. 4, 792–801.

[25] F. S. Marzano, D. Scaranari, and G. Vulpiani (2007), Supervised fuzzy-logic classification of hydrometers using C-band weather radars, *IEEE Trans. Geosci. Remote Sens.*, vol. 45, no. 11, 3784–3799.

[26] R. J. Doviak, and D. S. Zrnic (1993), Doppler Radar and Weather Observations, Second edition, chap. 6, 122–159, *Dover Publications, Inc., New York, U.S.*.

[27] A. D. Siggia, and R. E. Passarelli (2004), Gaussian model adaptive processing (GMAP) for improved ground clutter cancellation and moment calculation, *Proc. ERAD*, 67–73.

[28] C. M. Nguyen, D. N. Moisseev, and V. Chandrasekar (2006), Precipitation spectral moment estimation and clutter mitigation using parametric time domain model, *Proc. IGARSS*, 652–655.

[29] C. W. Helstrom (1995), Elements of Signal Detection and Estimation, *Prentice Hall, Englewood, NJ, U.S.*.

[30] E. Kreyszig (1999), Advanced Engineering Mathematics, *John Wiley and Sons Inc., Hoboken, NJ, U.S.*.

[31] T. Mega, K. Monden, T. Ushio, K. Okamoto, Z. Kawasaki, and T. Morimoto (2007), A low-power high-resolution broad-band radar using a pulse compression technique for meteorological application, *IEEE Geosci. Remote Sens. Lett.*, Vol. 4, 392–396.

[32] D. Atlas, R. C. Srivastava, and R. S. Sekhon (1973), Doppler radar characteristics of precipitation at vertical incidence, *Rev. Geophys.*, Vol. 11, 1–35.

[33] R. Schafer, S. Avery, P. May, D. Rajopadhyata, and R. Williams (2002), Estimation of rainfall drop size distributions from dual-frequency wind profiler spectra using deconvolution and a nonlinear least square fitting technique, *J. Atmos. Oceanic Technol.*, vol. 19, 864–874.

[34] C. Lucas, A. D. MacKinnon, R. A. Vincent, and P. T. May (2004), Raindrop size distribution retrieval from a VHF boundary layer profiler, *J. Atmos. Oceanic Technol.*, vol. 21, 45–60.

[35] R. J. Trapp and C. A. Doswell III (2000), Radar data objective analysis, *J. Atmos. Oceanic Technol.*, vol. 17, 105–120.

[36] P. T. May and D. K. Rajopadhyata (1996), Wind profiler observations of vertical motion and precipitation microphysics of a tropical squall line, *Mon. Weather Rev.*, vol. 124, 621–633.

[37] C. W. Ulbrich (1981), Natural variations in the analytical form of the raindrop size distribution, *J. Appl. Meteorol.*, vol. 22, 1764–1775.

[38] J. Testud, S. Oury, R. A. Black, P. Amayenc, and X. Dou (2001), The concept of "normarized" distribution to describe raindrop spectra: A tool for cloud physics and cloud remote sensing, *J. Appl. Meteorol.*, vol. 40, 1118–1140.

[39] T. Iguchi and R. Meneghini (1994), Intercomparison of single-frequency methods for retrieving a vertical rain profile for airborne or spaceborne radar data, *J. Atmos. Oceanic Technol.*, vol. 11, 843–863.

[40] W. Hitschfeld and J. Bordan (1954), Errors inherent in the radar measurement of rainfall at attenuation wavelength, *J. of Meteorol.*, vol. 11, 58–67.

[41] R. Meneghini (1978), Rain-rate estimates for an attenuating radar, *Radio Sci.*, vol. 13, 459–470.

[42] R. Meneghini, J. Eckerman and D. Atlas (1983), Determination of rain rate from a space-borne radar using measurements of total attenuation, *IEEE Trans. Geosci. Remote Sens.*, vol. 21, 34–43.

[43] R. Meneghini and K. Nakamura (1990), Range profiling of the rain rate by an airborne weather radar, *Remote Sens. Environ.*, vol. 31, 193–209.

[44] Z. S. Haddad, E. Im, S. L. Durden, and S. Hensley (1996), Stochastic filtering of rain profiles using radar, surface-referenced radar, or combined radar-radiometer measurements, *J. Appl. Meteorol.*, vol. 35, 229–242.

[45] C. R. Williams and K. S. Gage (2009), Raindrop size distribution variability estimated using ensemble statistics, *Ann. Geophys.*, vol. 27, 555–567.

[46] S. Haykin (1996), Adaptive Filter Theory, Third edition, chap. 7, 302–337, *S Simon and Schuster Company, Upper Saddle River, NJ, U.S.*.

List of Publications

Journal Papers

A.1 Yoshikawa, E., T. Mega, T. Morimoto, T. Ushio, and Zen Kawasaki (2009) Real-time spectral moments estimation and ground clutter suppression for precipitation radar with high resolution, *IEICE Transactions on Communication, E92-B*, 2, 578-584.

A.2 Yoshikawa, E., T. Mega, S. Yoshida, T. Morimoto, T. Ushio, Zen Kawasaki, K. Imai, and S. Nagayama (2010), Development and initial observation of high resolution volume scanning radar for meteorological application, *IEEE Transactions on Geoscience and Remote Sensing, 48*, 8, 3225-3235.

A.3 Yoshikawa, E., S. Kida, S. Yoshida, T. Morimoto, T. Ushio, and Zen Kawasaki (2010), Vertical structure of raindrop size distribution in lower atmospheric boundary layer, *Geophysical Research Letters, 37*, L20802, doi:10.1029/2010GL045174.

Proceedings of International Conferences

B.1 Ushio, T., E. Yoshikawa, T. Morimoto, and Zen Kawasaki, Broad band radar for high resolution observation of precipitation, IEEE Radar Conference, Rome, Italy, May 2008.

B.2 Yoshikawa, E., T. Mega, T. Morimoto, T. Ushio, and Zen Kawasaki, Development and Observation of the Ku-band Broad-band Radar for Meteorological Application, IEEE International Geoscience & Remote Sensing Symposium, Boston, July, 2008.

B.3 Yoshikawa, E., Y. Nakamura, T. Morimoto, T. Ushio, Zen Kawasaki, T. Mega, K. Imai, T. Nishida, T. Saito, and N. Sakazume, Rainfall observation with high resolution using Ku-band broad band radar, IEEE Radar Conference, Pasadena, USA, May, 2009.

B.4 Yoshikawa, E., S. Yoshida, T. Morimoto, T. Ushio, Zen Kawasaki, Initial Observation Results for Precipitation on the Ku-band Broadband Radar Network, IEICE International Conference on Space Aeronautical and Navigational Electronics, Jeju, Oct, 2010.

B.5 Yoshikawa, E., S. Yoshida, T. Morimoto, T. Ushio, Zen Kawasaki, Network Retrieval Technique for Precipitation Attenuation on Ku-band Broadband Radar Network, IEICE International Conference on Space Aeronautical and Navigational Electronics, Jeju, Oct, 2010.

Other Publications

C.1 Nakamura, Y., E. Yoshikawa, M. Akita, T. Morimoto, T. Ushio, Zen Kawasaki, T. Saito, T. Nishida, and N. Sakazume (2009), High-Resolution Precipitation and Lightning Monitoring by the Ku-band Broadband Radar and the VHF Broadband Digital Interferometer, *IEEJ Transactions on Fundamentals and Materials*, *129*, 12, 845-852.

C.2 Ushio, T., E. Yoshikawa, T. Morimoto, and Zen Kawasaki (2009), Kisyou Radar No Kogataka, *Kensa Gijutsu*, *14*, 7, 16-21 (in Japanese).

C.3 Ushio, T., E. Yoshikawa, M. Akita, Y. Nakamura, T. Morimoto, and Zen Kawasaki (2010), Raihouden To Sekiran-un No Koubunkainou Kansoku Gijutsu To Sono Kagaku, *Denki Gakkai Ronbunshi A*, *130*, 1, 10-14 (in Japanese).